

QUADRUPOLEAR MAGNETIC RECONNECTION IN SOLAR FLARES. I. THREE-DIMENSIONAL GEOMETRY INFERRED FROM *YOHKOH* OBSERVATIONS

MARKUS J. ASCHWANDEN

Lockheed Martin Advanced Technology Center, Solar and Astrophysics Laboratory, Department L9-41, Building 252, 3251 Hanover Street, Palo Alto, CA 94304; aschwanden@lmsal.com

TAKEO KOSUGI

Institute of Space and Astronautical Science, 3-1-1 Yoshinodai, Sagamihara, Kanagawa 229-8510, Japan

YOICHIRO HANAOKA

Nobeyama Radio Observatory, National Astronomical Observatory of Japan, Nobeyama, Minamimaki, Minamisaku, Nagano 384-13, Japan

MASANORI NISHIO

Department of Physics, Kagoshima University, 1-21-35 Kourimoto, Kagoshima, Kagoshima 890-0065, Japan

AND

DONALD B. MELROSE

Special Research Centre for Theoretical Astrophysics, School of Physics, University of Sydney, NSW 2006, Australia

Received 1999 February 26; accepted 1999 July 15

ABSTRACT

We analyze the three-dimensional geometry of solar flares that show so-called interacting flare loops in soft X-ray, hard X-ray, and radio emission, as previously identified by Hanaoka and Nishio. The two flare loops that appear brightest after the flare are assumed to represent the outcome of a quadrupolar magnetic reconnection process, during which the connectivity of magnetic polarities is exchanged between the four loop footpoints. We parameterize the three-dimensional geometry of the four involved magnetic field lines with circular segments, additionally constrained by the geometric condition that the two pre-reconnection field lines have to intersect each other at the onset of the reconnection process, leading to a 10 parameter model. We fit this 10 parameter model to *Yohkoh* Soft and Hard X-Ray Telescopes (SXT and HXT) data of 10 solar flares and determine in this way the loop sizes and relative orientation of interacting field lines before and after reconnection. We apply a flare model by Melrose to calculate the magnetic flux transfer and energy released when two current-carrying field lines reconnect to form a new current-carrying system in a quadrupolar geometry. The findings and conclusions are the following. (1) The pre-reconnection field lines always show a strong asymmetry in size, consistent with the scenario of newly emerging small-scale loops that reconnect with preexisting large-scale loops. (2) The relative angle between reconnecting field lines is nearly collinear in half of the cases, and nearly perpendicular in the other half, contrary to the antiparallel configuration that is considered to be most efficient for magnetic reconnection. (3) The angle between interacting field lines is reduced by $\approx 10^\circ$ – 50° after quadrupolar reconnection. (4) The small-scale flare loop experiences a shrinkage by a factor of 1.31 ± 0.44 , which is consistent with the scaling law found from previous electron time-of-flight measurements, suggesting that electron acceleration occurs near the cusp of quadrupolar configurations. (5) The large-scale loop is found to dominate the total induction between current-carrying loops, providing a simple estimate of the maximum magnetic energy available for flare energy release because of current transfer, which scales as $\Delta E^I \approx 10^{29.63} (r_2/10^9 \text{ cm})(I_2/10^{11} \text{ A})^2$ (with r_2 the curvature radius and I_2 the current of the large-scale loop) and is found to correlate with observed flare energies deduced from soft X-ray and hard X-ray fluxes. Most of the energy is transferred to small-scale loops that have one-half of the large-scale current ($I_1 = I_2/2$). (6) The quadrupolar reconnection geometry provides also a solution of Canfield's dilemma of the offset between the maximum of vertical currents and the HXR flare loop footpoints. (7) The quadrupolar geometry provides not only a framework for interacting double-loop flares, but it can also be considered as a generalized version of (cusp-shaped) single-loop flares.

Subject headings: MHD — Sun: flares — Sun: magnetic fields — Sun: X-rays, gamma rays

1. INTRODUCTION

Recent analysis of solar flare observations in soft X-rays (SXR), hard X-rays (HXR), and radio wavelengths have clearly revealed that often multiple loops are involved in the flare process. Detailed studies by Hanaoka (1996, 1997) and Nishio et al. (1997) have concentrated on cases with interacting flare loops. The typical configuration in such cases consists of a pair of two disjoint and unequal-sized flare loops (with a typical size ratio of 1:4), which share the same magnetic polarity at the more closely spaced footpoints, while the loop planes are oriented in some angle. This par-

ticular configuration has also been dubbed “three-legged structure” (e.g., Hanaoka 1997). Similar configurations with interacting flare loops have been observed earlier (e.g., the 1980 November 5 flare, described in Duijveman, Hoyng, & Machado 1982, Dennis 1985, Benz 1993, p. 146; the 1980 August 31 flare, described in Strong et al. 1984, Benz 1985; flares with remote footpoints of secondary flare loops, described in Nakajima et al. 1985, Hanaoka 1999; interacting loops described in Machado et al. 1988; or HXR/SXR/radio double loop structures in Kundu et al. 1995, Gopalswamy et al. 1995, Wang et al. 1995). Such geometries

of interacting flare loops cannot be described with a two-dimensional model (as they are simplified in some theoretical models) but rather require a full three-dimensional approach, which is the main subject of this study.

The interaction of magnetic field lines can be forced only by an external driver, e.g., by magnetic flux emerging from below the photosphere, by photospheric shear motion, by the kink instability of current-carrying loops, or by coronal large-scale reconfigurations. Once two magnetic field lines are brought into physical contact (or nearly so), a reconfiguration of magnetic connectivities can be facilitated, especially when the new configuration corresponds to a lower energy state and reduced magnetic tension. The simplest magnetic topology of such a process is a quadrupolar configuration, as illustrated in Figure 1 for a pair of two dipole-like field lines. Let us assume that a small field line (with footpoints labeled as $1+$, $1-$) is rising (e.g., driven by flux emergence or by footpoint shear motion) and pushes against a preexisting large-scale field line (with footpoints labeled as $2+$, $2-$; Fig. 1 left column). Once the two field lines approach each other sufficiently closely, the only possible way to reconfigure dipolar field lines is by exchanging the connectivities of opposite magnetic polarities, i.e., new field lines that connect footpoints ($1+$, $2-$) and ($1-$, $2+$). The newly configured field lines have initially a triangular cusp at the reconnection point, which may relax into a dipole-like geometry (visualized in Fig. 1, middle column). The final outcome of this quadrupolar reconnection process is two disjoint loops (Fig. 1, right). We apply this basic geometric model to the interpretation of observed flare configurations. The magnetic reconnection process is expected to occur at the Alfvénic speed (in the outflow region), which completes the relaxation episode of newly configured flare loops on timescales of ≈ 10 – 30 s for typical (compact) flare loop sizes. However, the detection of newly configured flare loops requires filling by heated plasma, e.g., by the chromospheric evaporation process, which occurs somewhat

slower, approximately at the sound speed. A consequence of this filling delay is therefore that the initial cusp shape after reconnection cannot be observed directly, while the flare loops become SXR-bright only during the dipolar relaxation phase. We expect therefore to see the disjoint, relaxed final loops only, but not the interacting field lines before reconnection. However, using the geometric concept outlined in Figure 1, we can easily reconstruct the pre-reconnection configuration by switching the connectivities of the magnetic polarities. This method is used here to explore the three-dimensional geometry of quadrupolar reconnection from observed data, which provides crucial parameters to test theoretical reconnection models. The obtained parameters are particularly suitable for application of a quadrupolar flare model developed by Melrose (1997), which describes the interaction between two current-carrying loops.

The three-dimensional geometry of our quadrupolar model is defined in § 2. This three-dimensional model is then fitted to *Yohkoh* Soft and Hard X-Ray Telescope (SXT and HXT) data of 10 flares (§§ 3.1–3.4). Part of the data analysis includes the application of the Melrose (1997) quadrupolar current-loop model (§ 3.5) and comparison of the resulting magnetic energies with flare energies estimated from *GOES* SXR and *Yohkoh* HXR fluxes (§ 3.6). Based on these results we obtain a simple approximation of Melrose’s model (§ 4.1). We discuss our results in the context of previous concepts of quadrupolar flare models (§ 4.2), the role of large-scale currents (§ 4.3), and shear angles of flare loops (§ 4.4). Conclusions are summarized in § 5.

2. THREE-DIMENSIONAL GEOMETRY MODEL

2.1. Loop Definitions

The three-dimensional geometry of magnetic field lines involved in a quadrupolar reconnection process requires the definition of four field lines, i.e., 2 field lines before and 2

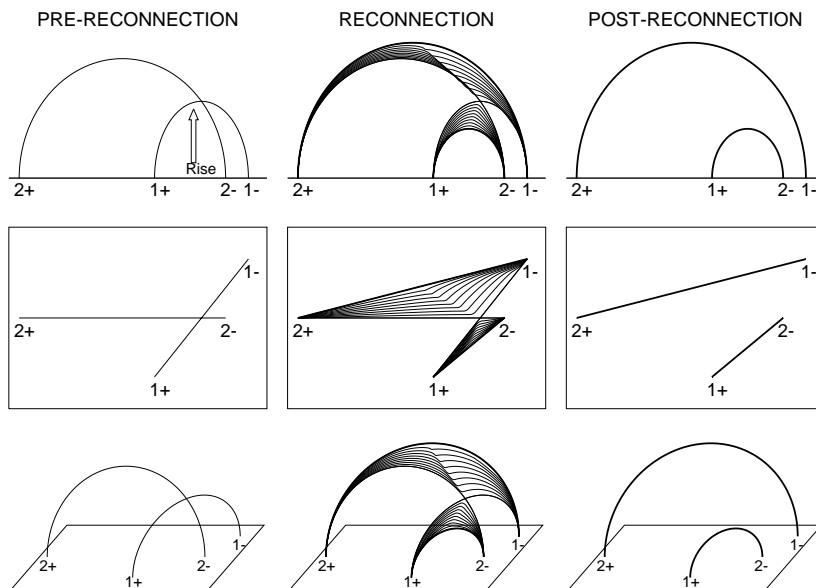


FIG. 1.—Concept of magnetic reconnection in a quadrupolar geometry visualized for two semicircular loops (1 and 2) with initial footpoints ($1+$, $1-$) and ($2+$, $2-$). The three stages, (left column) pre-reconnection, (middle column) main reconnection with subsequent relaxation process, and (right column) final post-reconnection, are depicted for three different views, i.e., (top row) side view, (middle row) top view, and (bottom row) perspective view. Note that all loop shapes in the initial and final phases are represented by circular segments, while the intermediate stages of the relaxing field lines are rendered by linear interpolation.

after reconnection, anchored interchangeably in the same four footpoints. We denote the footpoint coordinates in a plane parallel to the solar surface by Cartesian coordinates (x_{1+}, y_{1+}) , (x_{1-}, y_{1-}) for the smaller loop 1, and by (x_{2+}, y_{2+}) , (x_{2-}, y_{2-}) for the larger loop 2 (Fig. 2, lower left). For convenience, we refer to the newly configured field lines with interchanged polarities as loop 3 and 4, with footpoint coordinates $(x_{3+} = x_{1+}, y_{3+} = y_{1+})$, $(x_{3-} = x_{2-}, y_{3-} = y_{2-})$ for loop 3 (generally the smaller one of the two new loops), and footpoint coordinates $(x_{4+} = x_{2+}, y_{4+} = y_{2+})$, $(x_{4-} = x_{1-}, y_{4-} = y_{1-})$ for loop 4. The midpoints of the loop footpoint baselines have the following coordinates for these four loops $i = 1, \dots, 4$

$$x_i = \frac{1}{2}(x_{i+} + x_{i-}), \quad i = 1, \dots, 4, \quad (1)$$

$$y_i = \frac{1}{2}(y_{i+} + y_{i-}), \quad (2)$$

while the length B_i of the loop baseline has the value

$$B_i = \sqrt{(x_{i+} - x_{i-})^2 + (y_{i+} - y_{i-})^2}, \quad i = 1, \dots, 4, \quad (3)$$

which corresponds to the diameter of the loop curvature in the case of a semicircular geometry. A semicircular geometry with a vertical loop plane represents a minimal parametrization of a loop with four parameters, which can be expressed by the loop midpoint (x_i, y_i) , the loop radius $r_i = B_i/2$, and the azimuthal angle \mathcal{G}_i of the footpoint baseline to the x -axis of the Cartesian coordinate system,

$$\mathcal{G}_i = \arctan \left(\frac{y_{i+} - y_{i-}}{x_{i+} - x_{i-}} \right). \quad (4)$$

The same geometric definitions are also used in a quadrupolar model of Melrose (1997; § 3.1), where two additional parameters are introduced, namely, the relative angle

between two loops i and j ,

$$\mathcal{G}_{ij} = \mathcal{G}_i - \mathcal{G}_j, \quad (5)$$

and the distance, d_{ij} , between the centers (x_i, y_i) of the loops i and j ,

$$d_{ij} = \sqrt{(x_i - x_j)^2 + (y_i - y_j)^2}. \quad (6)$$

For the data analysis here it turns out that a semicircular approximation with vertical loop planes is appropriate for the smaller flare loops, because only the footpoint coordinates can be accurately measured from HXR images (constraining four parameters), while the larger flare loops seen in SXR images show sometimes significant deviations from vertical loop planes or from a semicircular geometry. Thus we introduce two additional parameters for the larger loops, i.e., the inclination angle ζ_i of the loop plane to the vertical and an offset Δr_i of the circular loop center from the baseline. We approximate the large loops still with circular segments but allow the circular center to be located above or below the solar surface. For a given footpoint separation B_i and circular offset Δr_i , the loop curvature radius r_i is then defined by

$$r_i = \sqrt{(B_i/2)^2 + (\Delta r_i)^2}. \quad (7)$$

A small-scale loop requires thus four free parameters, and a large-scale loop six free parameters, leading to a total of 10 geometric loop parameters in our model.

2.2. Reconnection Condition

Magnetic X-type reconnection requires the intersection of two field lines at some angle. This physical criterion imposes an additional geometric criterion that reduces the number of free parameters. Let us denote the reconnection point with the three-dimensional Cartesian coordinates (x_R, y_R, z_R) , which is required to be a common location for both interacting field lines. Because we deal here with a special configuration where a small-scale field line rises and interacts with an overlying large-scale preexisting field line, it is most likely that the interaction occurs near the apex of the small-scale field line, which is in closest proximity to an overlying field (see Fig. 2). Because we approximate the small-scale field line 1 with a vertical semicircular geometry (with radius r_1), the coordinates of the reconnection point are given by the midpoint of its baseline at (x_1, y_1) and by its radius r_1 ,

$$(x_R, y_R, z_R) = (x_1, y_1, r_1). \quad (8)$$

This reconnection point constrains an additional point $[x_2(\varphi_R) = x_R, y_2(\varphi_R) = y_R, z_2(\varphi_R) = z_R]$ of the large-scale loop 2 (defined by the circular angle φ_R of the reconnection point in our loop parametrization; see eqs. [A1]–[A3]) and thus reduces its six free parameters to essentially three parameters.

2.3. Numerical Parameter Determination

What the data allow us to measure are the geometric parameters of the final flare loops (3 and 4) in the post-reconnection phase. Based on the work of Hanaoka (1996, 1997) and Nishio et al. (1997), we know that the compact flare loop often shows a pair of double HXR sources, from whose centroids we can determine the footpoints of the small-scale loop, (x_{1+}, y_{1+}) and (x_{2-}, y_{2-}) , leading to its

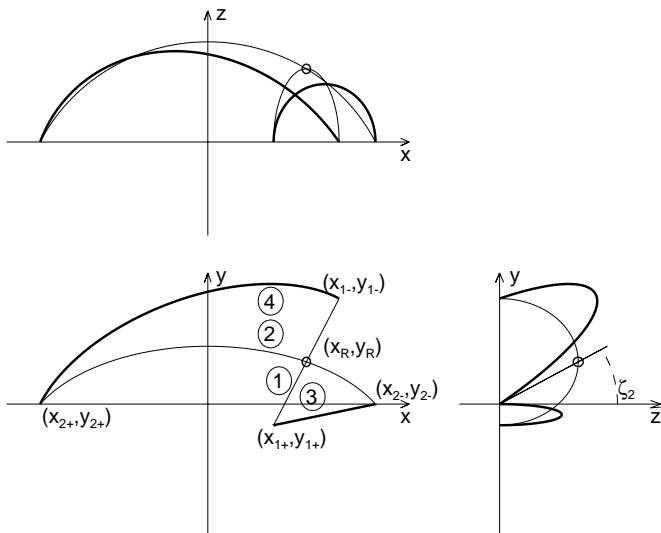


FIG. 2.—*Top panel*: Definition of some geometric parameters in the vertical x - z plane. *Lower right panel*: Vertical y - z plane. *Lower left panel*: Horizontal x - y plane. Pre-reconnection field lines are drawn with thin lines, post-reconnection field lines with thick solid lines, and the X-point reconnection point (x_R, y_R, z_R) is marked with a small circle. The footpoint positions (x_{1+}, y_{1+}) and (x_{1-}, y_{1-}) refer to the small-scale loop, and the footpoint positions (x_{2+}, y_{2+}) and (x_{2-}, y_{2-}) refer to the large-scale loop. The inclination angle of the loop plane ζ_2 is indicated in the y - z plane. Note the numeration of loops, i.e., “1,” “2” for pre-reconnection field lines, and “3,” “4” for post-reconnection field lines, respectively.

four-parameter characterization [midpoint (x_3, y_3) , azimuth \mathcal{G}_3 and radius $r_3 = B_3/2$]. For the large-scale flare loop, it is generally easy to measure the location of the remote footpoint (x_{2+}, y_{2+}) (associated with positive polarity in the example shown in Fig. 2), but the location of the opposite footpoint near the smaller flare loop is subject to large uncertainties because the bright SXR emission in the immediate neighborhood of the flare kernel generally blurs the location of individual SXR loop footprints. We are therefore left with two measurable parameters (x_{2+}, y_{2+}) and four free variables $(x_{1-}, y_{1-}, \zeta_1, \Delta r_1)$ for the large-scale flare loop 4. In the following data analysis we determine the four free variables of the large-scale loop 4 by tracing a number ($m = 3-5$) of additional loop positions $(x_{2j}, y_{2j}, j = 1 \dots m)$ along the loop, to which the geometric loop model $[x_L(\varphi), z_L(\varphi)]$ (eqs. [A1]–[A4] in the Appendix) is fitted. The optimization of the four free variables $(x_{1-}, y_{1-}, \zeta_1, \Delta r_1)$ is accomplished by minimizing the combined least-squares deviations $\sigma^2 = \sigma_F^2 + \sigma_R^2$, consisting of (1) the least-squares deviations of the model from the large-scale flare loop positions,

$$\sigma_F^2 = \sum_{j=1}^m [x_{2j} - x_2(\varphi_j)]^2 + [y_{2j} - y_2(\varphi_j)]^2, \quad (9)$$

and (2) the coordinate differences at the intersection point of loop 1 and 2 (according to the reconnection condition given in equation (8), $x_R = x_1, y_R = y_1, z_R = r_1$),

$$\sigma_R^2 = \sum_{j=1}^m [x_R - x_2(\varphi_R)]^2 + [y_R - y_2(\varphi_R)]^2 + [z_R - z_2(\varphi_R)]^2, \quad (10)$$

where φ_j and φ_R are determined by a first minimization in φ -parameter space. The four-parameter minimization is performed here with the Powell method (Press et al. 1986, pp. 294–300). In summary, our model-fitting procedure consists of the measurement of three footpoints (constraining six model parameters) and a four-parameter optimization, which constrains a total of 10 model parameters. The small-scale flare loop is characterized by $(x_3, y_3, \mathcal{G}_3, r_3)$ and the large-scale flare loop by $(x_4, y_4, \mathcal{G}_4, r_4, \Delta r_4, \zeta_4)$.

The 10 parameters of the pre-reconnection field lines (1 and 2) are then retrieved by using equations (1)–(4) and making the additional assumption that the inclination angle and loop center offset of the large-scale loop remains unchanged during reconnection ($\Delta r_2 \approx \Delta r_4$ and $\zeta_2 \approx \zeta_4$). This assumption can be justified by the fact that the large loops change their position only by a small angle, which becomes smaller the larger the size ratio is between the small and large loops. The pre-reconnection field lines are then fully constrained by the 10 parameters: $(x_1, y_1, \mathcal{G}_1, r_1)$ and $(x_2, y_2, \mathcal{G}_2, r_2, \Delta r_2, \zeta_2)$.

The definition of loop coordinates (x, y, z) is described here in the framework of Cartesian coordinates, where the x - y plane is parallel to the solar surface. For the practical part of the data analysis, these loop coordinates (x, y, z) have also to be transformed into heliographic coordinates (l, b, r) (eq. [A5] in the Appendix) and into image coordinates (X, Y) (eq. [A6] in the Appendix) as they appear in the plane of sky. For the optimization problem described above, the backward transformations, which can be derived straightforwardly from equations (A1)–(A6) in the Appendix, are also needed.

2.4. Relaxation Scaling Ratio

In our quadrupolar reconnection flare model, the energy release occurs during the relaxation phase, when the newly configured field lines with initial cusp shapes relax to dipole-like shapes (with near-circular geometry). Flare heating and particle acceleration is presumably associated with the changes of the magnetic field during this relaxation phase, which occurs fastest in the cusp area. The specific geometry defined in our model allows us to determine the maximum propagation distance of (nonthermal) particles that are accelerated in the cusp region and propagate to the chromospheric footpoints, which can be compared with particle time-of-flight measurements (e.g., Aschwanden et al. 1996). It is therefore useful to determine the scaling ratio of cusp-shaped field lines (at onset of reconnection) to dipole-like field lines (in the final post-reconnection phase).

The lengths of the three-dimensional cusp-shaped field lines can simply be determined in our model by combining the corresponding two-dimensional circular loop segments of the pre-reconnection phase. The lengths l_i of the newly configured cusp field lines is thus

$$l_3 = r_1 \left(\frac{\pi}{2} \right) + r_2(\varphi_R - \varphi_{0,2}), \quad (11)$$

$$l_4 = r_1 \left(\frac{\pi}{2} \right) + r_2(\pi - \varphi_R - \varphi_{0,2}), \quad (12)$$

while the lengths l'_i of the relaxed newly configured (circular) field lines are

$$l'_3 = r_3 \pi, \quad (13)$$

$$l'_4 = r_4(\pi - 2\varphi_{0,4}), \quad (14)$$

where $\varphi_{0,i}$ is defined by equation (A3) and φ_R represent the circular angle corresponding to the reconnection point in loop 2, which can be obtained from equations (8) and (A1)–(A4),

$$\varphi_R = \arcsin \left(\frac{r_1}{r_2 \cos \zeta} - \frac{\Delta r_2}{r_2} \right). \quad (15)$$

The length ratios q_i of the initial to the final field lines during the quadrupolar relaxation phase are then defined by

$$q_3 = l_3/l'_3, \quad (16)$$

$$q_4 = l_4/l'_4. \quad (17)$$

A simple analytical expression can be given for the special case of extreme loop size ratios ($r_1 \ll r_2$) (for semicircular loops $\Delta r_i = 0$ with vertical loop planes $\zeta = 0$). In this approximation we obtain $\varphi_{2,0} = 0$ (eq. [A3]), $\varphi_R \approx r_1/r_2$ (eq. [15]), and $r_3 \approx r_1/2$ (because $x_1 = x_R \approx x_{2-}$ and $y_1 = y_R \approx y_{2-}$), yielding (with eqs. [11], [13], [16])

$$q_3(r_1 \ll r_2) \approx (1 + 2/\pi) = 1.64, \quad (18)$$

$$q_4(r_1 \ll r_2) \approx 1. \quad (19)$$

Thus, the small-scale flare loop experiences in this case a significant shrinkage (q_3), while the large-scale flare loop maintains its length ratio (q_4).

2.5. Shear Reduction

For a symmetric dipole field, the neutral line runs orthogonal to the dipolar axis (which connects the two poles). In

some models, the buildup of nonpotential magnetic energy that ultimately may be dissipated in a flare has been arranged by shearing of the magnetic field, driven by oppositely directed footpoint motion of dipolar loops in parallel and antiparallel directions to the neutral line (e.g., Klimchuk, Sturrock, & Yang 1988; Klimchuk & Sturrock 1992). Once the sheared magnetic field exceeds a critical angle, a flare can be triggered by the tearing-mode instability (Sturrock 1966), which consumes a fraction of the nonpotential magnetic energy and should lead to an end state with less free magnetic energy, corresponding to a reduced shear angle. It is therefore instructive to test whether the observations are consistent with this theoretical prediction of shear angle reduction after the flare. This flare scenario can be applied to our quadrupolar geometry, where the large-scale field line represents the unsheared field, while the small-scale field line is subjected to photospheric shear motion during the pre-reconnection phase (Aschwanden 1999). This scenario is an alternative to the emerging flux model.

In our quadrupolar model, we can define a shear angle by the angle between the pre-reconnection field lines, $\mathcal{G}_{12} = \mathcal{G}_1 - \mathcal{G}_2$ (eq. [5]), which changes to $\mathcal{G}_{34} = \mathcal{G}_3 - \mathcal{G}_4$ after reconnection. The resulting change in shear is therefore

$$\Delta\mathcal{G} = |\mathcal{G}_{34}| - |\mathcal{G}_{12}|, \quad (20)$$

which should be negative if shear is reduced by the reconnection process. Indeed, if the pre-reconnection configuration consists of intersecting baselines, it can be shown geometrically that the reconnection process always produces disjoint baselines with reduced shear. Without loss of generality, we can rotate the coordinate system by angle \mathcal{G}_2 so that $\mathcal{G}'_i = \mathcal{G}_i - \mathcal{G}_2$ and require a positive definition of $\mathcal{G}'_1 - \mathcal{G}'_2 > 0$. In the rotated configuration we have then $\mathcal{G}'_2 = 0$ and the inequalities $\mathcal{G}'_1 > 0$, $0 < \mathcal{G}'_3 < \mathcal{G}'_1$ and $0 < \mathcal{G}'_4 < \mathcal{G}'_1$ (see e.g., Fig. 1). It follows then directly that $\Delta\mathcal{G}' = |\mathcal{G}'_3 - \mathcal{G}'_4| - |\mathcal{G}'_1 - \mathcal{G}'_2| < 0$. Thus, our quadrupolar reconnection model always predicts a shear reduction

$$\Delta\mathcal{G} < 0 \quad (21)$$

and disjoint loops after reconnection. We verify this prediction with observational values in § 3.4 (see quadrupolar angles).

3. DATA ANALYSIS

3.1. Data Selection

We use the combined data set previously analyzed by Hanaoka (1996, 1997) and Nishio et al. (1997), which contains flare events with similar characteristics, namely, cases with interacting flare loops that have been identified by their HXR, SXR, and radio emission. This combined data set contains 24 events and is compiled in Table 1, which includes the references and relevant figures in the cited studies. We list also the *GOES* class and HXT count rate (in the M1 channel) to give an indicator of the importance and magnitude of these flares. We classify the morphology of the HXR source structures according to single (S), double (D), and multiple (M) sources (in the seventh column of Table 1). Some flares showing an elliptical source structure (E) are partly classified as double sources (D) if the elliptical brightness distribution can be unambiguously decomposed into two Gaussian sources. For our analysis we require an unambiguous identification of two interacting flare loops,

ideally constrained (1) by double HXR footpoint sources for the primary small-scale flare loop, and (2) by an SXR loop that extends to the remote footpoint of the secondary large-scale flare loop. We find 10 events (out of 24) that fulfill the two requirements for flare loop identification (marked with asterisks in Table 1). We do not make use of (Nobeyama) radio data here because the amorphous contours of the radio sources are not suitable for our analysis. Our selection of events may be biased toward larger primary flare loops, because smaller primary flare loops may appear as single sources that are excluded here.

3.2. Observations

We use *Yohkoh* images from the HXT (Kosugi et al. 1991), which is a Fourier-synthesis-type imager that makes two-dimensional solar images in four energy bands: low (13.9–22.7 keV), M1 (22.7–32.7 keV), M2 (22.7–32.7 keV), and high (52.7–92.8 keV). The spatial resolution is $\approx 5''$, and the highest temporal resolution is 0.5 s in flare mode. We synthesize the HXR images by integrating over the entire duration of the main flare peak, using the new modulation patterns (Sato et al. 1999) and the maximum entropy method (MEM). Details on the HXT data are also described in the new HXT Image Catalogue (Sato et al. 1998) and in previous publications (e.g., Nishio et al. 1997).

Additionally we use SXR images from the *Yohkoh* SXT (Tsuneta et al. 1991). The angular resolution of SXT is $2''.45$ in full resolution mode. We selected SXT images around the peak time of the HXT images, or some minutes later in cases when the brightness of the secondary flare loop was below detection threshold at the time of the HXR peak. The HXT and SXT images have been co-aligned from first principles using the solar center position provided in the latest spacecraft attitude files (status of January 1999) without further correction. The co-alignment is believed to be accurate to within $\approx 1''$ – $2''$ near disk center and somewhat worse near the limb.

3.3. Model Fitting

The results of our model fitting to the 10 selected flares is shown in Figure 3 and in Table 2. For each of the 10 flares we show four displays in Figure 3: the original co-aligned SXT and HXT images (*top row*), the best-fit model of SXT and HXT brightness distributions resulting from our three-dimensional model (*second row*), a vertical projection of the magnetic field line configuration of our three-dimensional model (*third row*), and a side projection of the same field lines (*fourth row*). The procedure of our model fitting is the following. First we measure the footpoint positions of the primary flare loop and several positions of the secondary flare loop, including the remote footpoint. The connectivity of quadruple magnetic polarities (see Fig. 1) allows in principle two possibilities, but the additional reconnection condition (eq. [8]) has only one physical solution in many cases (warranted by minimizing σ_R [eq. (10)] in our algorithm). In cases with two physical solutions, our algorithm yields that solution that is more consistent with the observed morphology of SXR loops (warranted by minimizing σ_F [eq. (9)] in our algorithm). The consistency of the magnetic polarities obtained from our model with magnetogram data will be tested in Paper II of this series. This numerical input of the measured positions is then processed according to the algorithm described in § 2.3 to infer the 10 model parameters of post-reconnection flare loops 3 and 4, $(x_3, y_3, \mathcal{G}_3, r_3)$ and

TABLE 1
DATA SET OF SOLAR FLARES WITH INTERACTING LOOPS

Number	Date	Time (UT)	GOES Class	Flare Duration ^a (s)	HXT/M1 ^b (counts s ⁻¹ SC ⁻¹)	HXR Source Structure ^c	Small Loop Identification ^d	Large Loop Identification ^d	Selection ^e	References
1	1992 Jun 25	03:34	C1.8	26	23	S	...	SXR	...	1 (Fig. 1), 2
2*	1992 Jul 15	02:00	C4.2	108	12	D	HXR, SXR	HXR, SXR	Y	1 (Fig. 1)
3*	1992 Aug 20	03:51	C4.5	174	12	D	HXR	SXR	Y	1 (Figs. 1, 4, 6)
4	1992 Aug 21	00:18	M1.3	SXR	(Radio)	...	3 (Fig. 6)
5*	1992 Sep 11	02:59	M1.0	(100)	31	D	HXR	SXR	Y	1 (Fig. 1)
6	1992 Sep 11	06:04	M1.4	534	93	S	1 (Fig. 1)
7	1992 Oct 23	01:03	M4.1	...	6	(Radio)	...	3 (Fig. 7)
8*	1992 Oct 29	06:32	C2.1	44	17	D	HXR	SXR	Y	1 (Fig. 1)
9	1992 Nov 05	06:19	M2.0	382	36	S	...	(Radio)	...	1 (Fig. 1)
10	1992 Dec 15	01:13	C6.9	362	30	S	...	SXR	...	1 (Fig. 1)
11*	1992 Dec 16	03:25	C4.6	288	13	D	HXR	SXR	Y	4 (Figs. 3, 16)
12	1992 Dec 16	06:05	C4.7	...	9	SXR	...	4 (Fig. 9)
13	1993 Feb 06	05:25	C5.6	...	23	(Radio)	...	1 (Fig. 1), 3 (Fig. 5)
14	1993 Apr 10	23:35	C9.1	116	38	S	...	SXR	...	1 (Fig. 1), 3 (Fig. 3)
15	1993 Apr 11	00:30	C6.2	3
16*	1993 Apr 11	06:16	C8.9	449	26	D	HXR	SXR	Y	3 (Fig. 9)
17	1993 May 28	02:02	C9.1	418	25	D	HXR	(Radio)	...	1 (Fig. 1), 2
18*	1993 Jun 07	05:42	C4.1	182	16	E	HXR	SXR	Y	1 (Fig. 1), 2, 3 (Fig. 1)
19	1993 Sep 30	22:43	C1.7	(Radio)	...	3 (Fig. 4)
20*	1993 Nov 30	06:03	C9.2	(100)	70	M	HXR	SXR, HXR	Y	1 (Fig. 1), 2, 5 (Fig. 3)
21*	1994 Jan 06	04:05	C4.9	140	24	D	HXR	SXR	Y	1 (Figs. 1, 8, 9, 10), 2
22*	1994 Jan 26	05:40	C1.4	42	59	S	HXR, SXR	HXR, SXR	Y	1 (Figs. 1, 12, 13), 2
23	1994 Dec 14	00:07	C4.8	752	5	S	3
24	1994 Dec 14	05:41	M2.5	(Radio)	...	3 (Fig. 8)

^a Duration of HXR, according to start time and end time given in HXT Catalogue (Sato et al. 1998). In two cases, shown in parentheses, the flare showed multiple HXR peaks and the duration was reduced to the duration of the relevant peak.

^b In units of counts s⁻¹ subcollimator⁻¹, background subtracted.

^c Source structure: ... = no HXT flare mode data, S = single source, E = elliptical source, D = double source, and M = multiple sources.

^d Images on which the identification of the small-scale flare loop is made by: HXR = Hard X-ray image from *Yohkoh*/HXT; SXR = Soft X-ray image from *Yohkoh*/SXT, and radio = Nobeyama radio image at 17 GHz (not used here)

^e Events selected for data analysis here are marked "Y" (see Fig. 3 and Table 2), based on unambiguous identification of both interacting flare loops

REFERENCES.—(1) Nishio et al. 1997; (2) Aschwanden et al. 1996; (3) Hanaoka 1997; (4) Hanaoka 1996; (5) Sylwester & Sylwester 1998. Relevant figures in the cited references are indicated in parentheses.

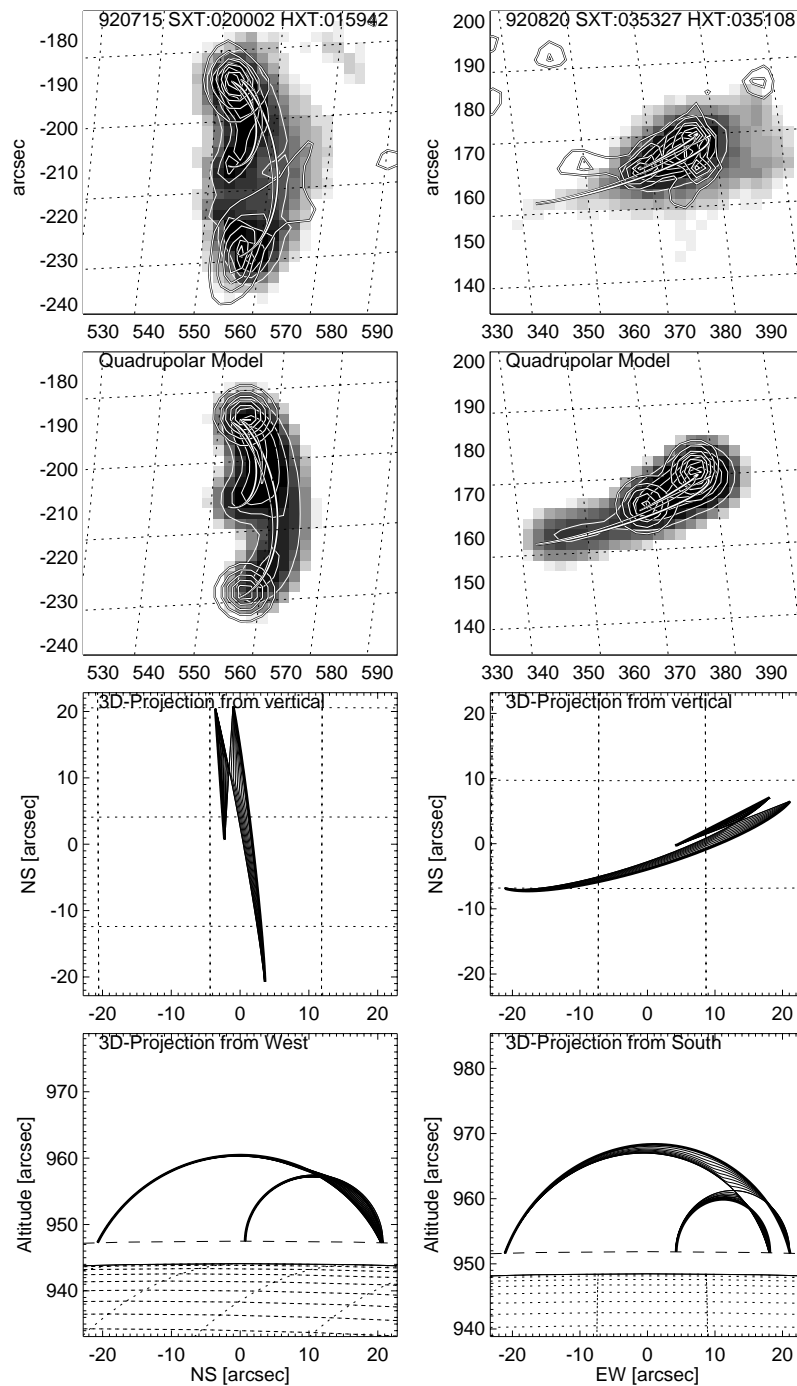


FIG. 3.—Data and three-dimensional quadrupolar model fit for the 10 analyzed flares. *Top row in each set*: Soft X-ray image (*logarithmic gray scale and thin contours*) from *Yohkoh/SXT* and hard X-ray image (*thick contours*) from *Yohkoh/HXT*. The thin circular segments represent the geometric solutions of the pre-reconnection field lines, and the thick circular segments show the corresponding post-reconnection field lines, which coincide with the flare loops. *Second row*: Simulated SXR and HXR maps constrained by the three-dimensional quadrupolar model, represented with identical gray scales and contour levels as the original data (*top row*). *Third row*: Geometric solution of the three-dimensional quadrupolar model rotated so that the vertical z -axis coincides with the line of sight. Ten field lines are interpolated between the pre- and post-reconnection state, visualizing the relaxation process of field lines after reconnection. *Bottom row*: Same three-dimensional grid model rotated so that either the x -axis (viewed from west) or the y -axis (viewed from south) coincides with the line of sight. The spacing of the heliographic grid is 1° (corresponding to 12,150 km) in all frames.

$(x_4, y_4, \mathcal{G}_4, r_4, \Delta r_4, \zeta_4)$, which can be equivalently expressed (by exchanging the combination of footpoint positions) in terms of the 10 parameters that define the pre-reconnection field lines 1 and 2, $(x_1, y_1, \mathcal{G}_1, r_1)$ and $(x_2, y_2, \mathcal{G}_2, r_2, \Delta r_2, \zeta_2)$. The numerical values of these geometric parameters are given in Table 2, where the (mid-baseline) loop positions (x_i, y_i) are given in heliographic coordinates (l_i, b_i) . Uncer-

tainties have been estimated for all measured parameters by repeating the position measurements and model fitting three times and by calculating the means and standard deviations from these three trials. The scatter mainly reflects uncertainties in pinpointing the centroids of HXR footpoint positions (particularly for elliptical or overlapping HXR sources) and SXR loop features (because of their amorp-

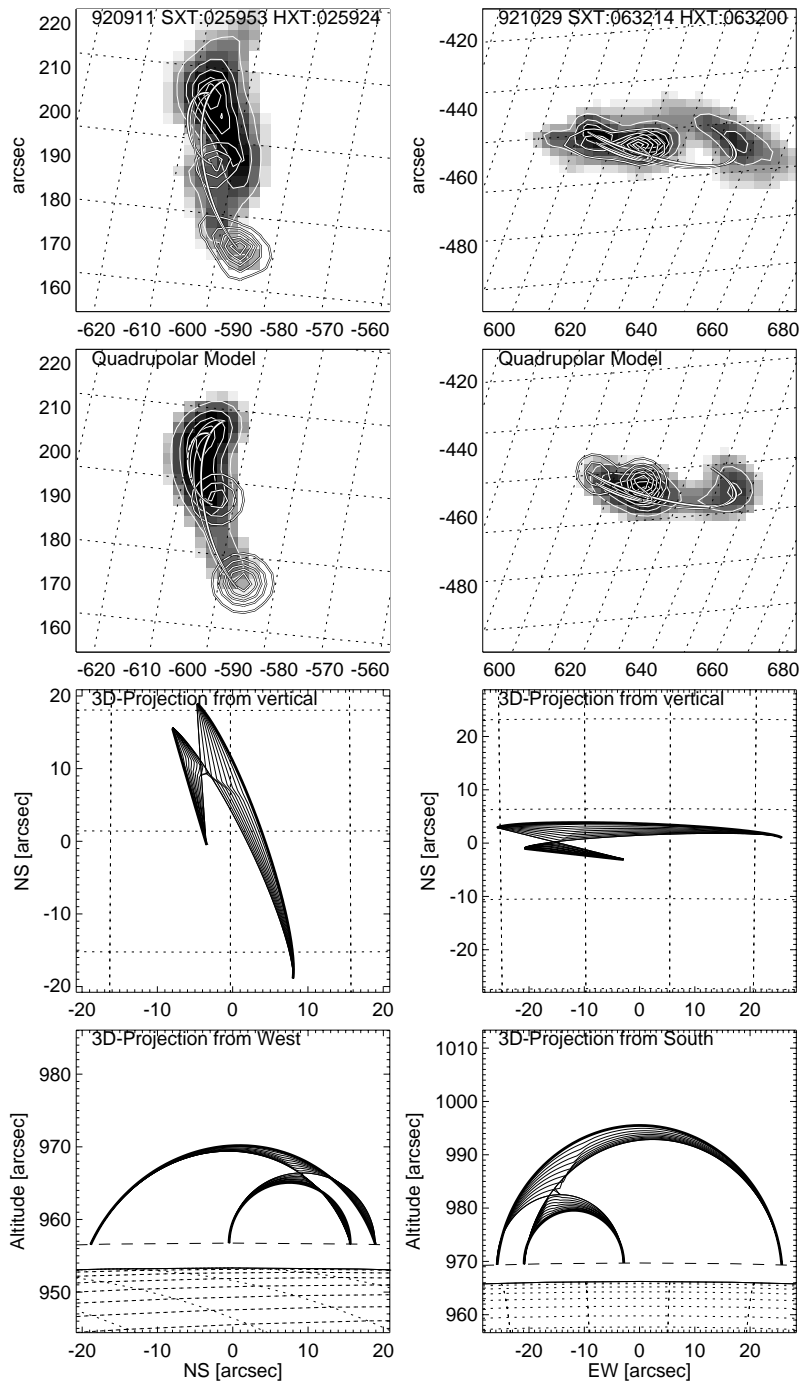


FIG. 3.—Continued

hous shapes). Typical uncertainties are $\sigma_{l,b} \lesssim 0.1$ for heliographic positions, $\sigma_r \approx 0.5\text{--}2''$ for loop radii, $\sigma_\theta \approx 2^\circ\text{--}4^\circ$ for azimuth angles of small-scale loops, $\sigma_\theta \approx 1^\circ\text{--}2^\circ$ for azimuth angles of large-scale loops, and $\sigma_\zeta \approx 1^\circ\text{--}7^\circ$ for inclination angles.

The representation of flare data in Figure 3 contains a gray-scale plot of the SXR map with contours (*thin lines*, scaled logarithmically in flux), together with the (linear) contours (*thick lines*) of the HXR map (*first row* in Fig. 3). In the model brightness distribution constrained by our three-dimensional model (second row in Fig. 3), we produce the HXR contours by convolution of the four footpoints of the quadrupolar configuration with Gaussian functions with half-width $5''$, scaled by the peak flux of the corre-

sponding HXR sources at identical positions in the original HXT maps. The SXR loops in our model brightness distribution (*second row* in Fig. 3) are rendered by convolving the magnetic field lines of loops 3 and 4 with Gaussian functions of uniform density along the field lines, with width roughly adjusted to the observed loop diameters (typically with Gaussian half-widths of 2 SXT pixels). The peak fluxes of the two loops are again adjusted to the actually observed peak fluxes at identical positions in the original maps.

3.4. Quantitative Results

Quadrupolar angles.—From the vertical projections shown in Figure 3 (*third row*) and Table 2, we see that the initial angles between pre-reconnection field lines have no

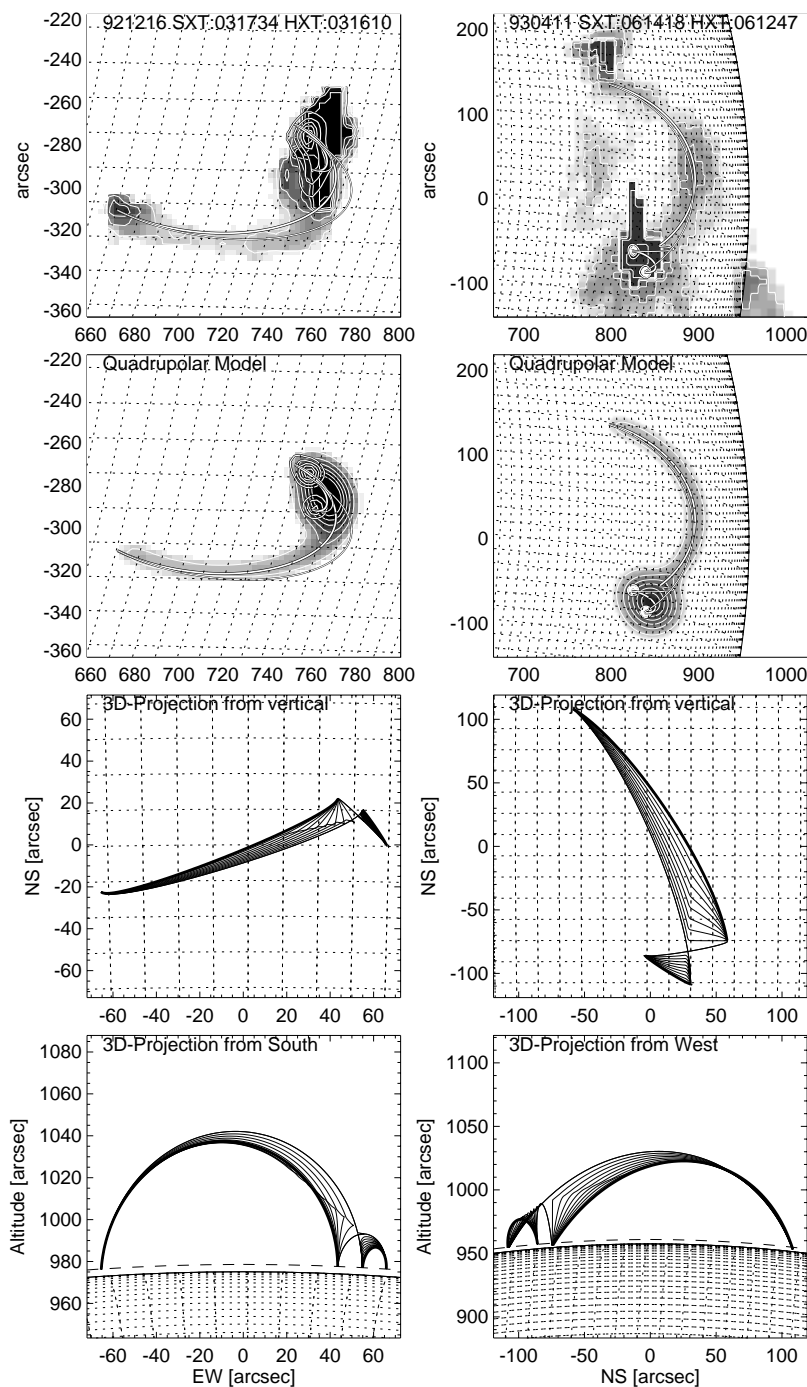


FIG. 3.—Continued

preferred range: six cases with almost collinear loops ($|\mathcal{G}_{12}| < 22^\circ$) are found, while the other four cases have more perpendicular angles ($60^\circ < |\mathcal{G}_{12}| < 141^\circ$). We did not find antiparallel loops, as they are generally thought to be most efficient for magnetic reconnection. The angles between the post-reconnection flare loops are generally similar to the angles before reconnection, except for some amount of “shear reduction” as predicted by our model (§ 2.5). The shear reduction $\Delta\mathcal{G}$ is negative in six of the 10 analyzed cases, as predicted by our model, while it is slightly positive in the four remaining cases because of significant inclination angles of the loop planes. If we calculate the

shear angle at the reconnection point (instead of between the baselines), the change in shear angle would always be negative. In our set of analyzed flares, the shear reduction amounts to $\Delta\mathcal{G} \approx -10^\circ, \dots, -50^\circ$.

Loop size ratios.—In Table 2 we list various scaling ratios. The length ratio of the large to the small pre-reconnection field line varies in the range $r_2/r_1 = 1.51, \dots, 4.11$ and has a mean of $r_2/r_1 = 2.6 \pm 0.9$. The ratio of the large to the small post-reconnection field lines has similar values, i.e., $r_4/r_3 = 1.83, \dots, 7.39$, with a mean of $r_4/r_3 = 3.9 \pm 1.9$, which is also similar to the ratio specified by Nishio et al. (1997), who list $r_4 = 30''\text{--}80''$ and $r_3 \leq 20''$

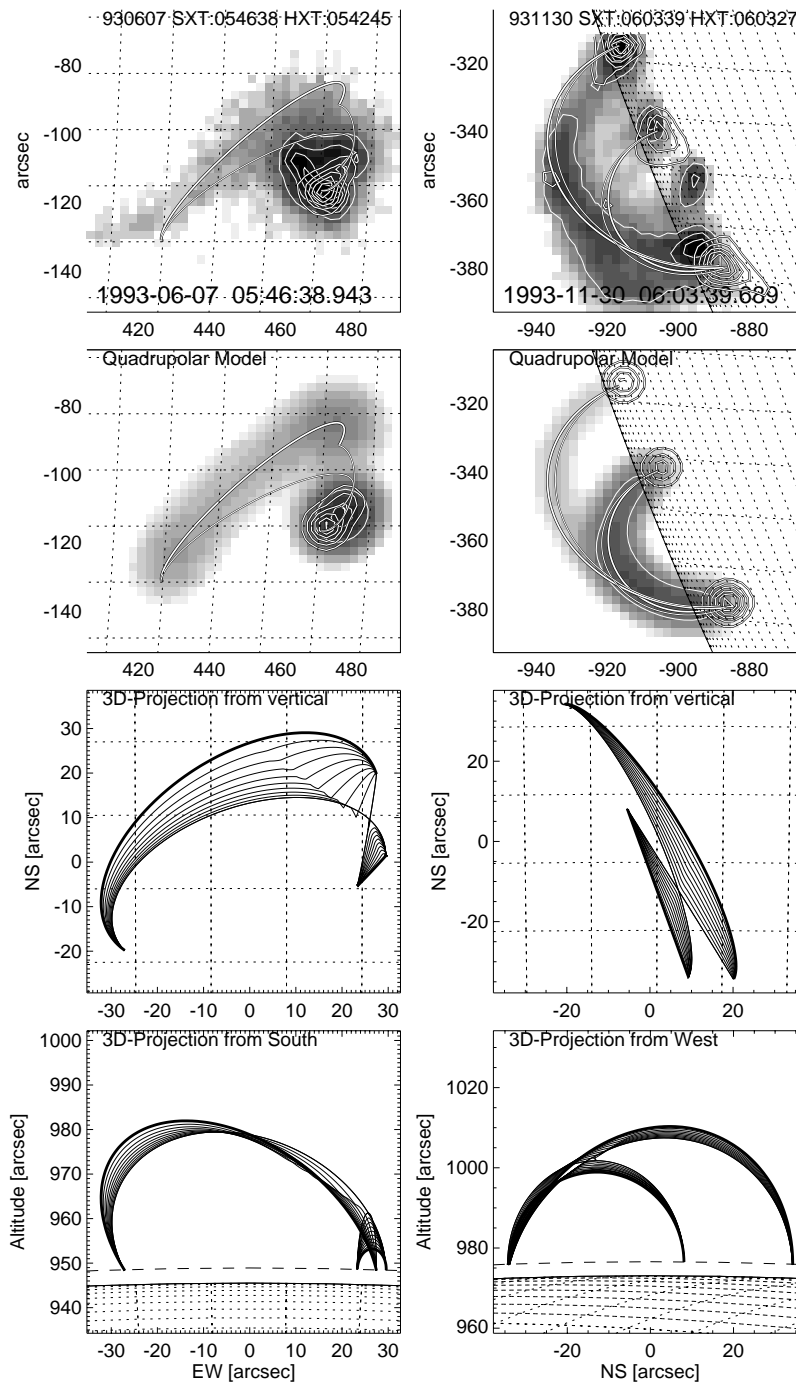


FIG. 3.—Continued

(yielding a ratio of $r_4/r_3 \geq 1.5, \dots, 4.0$). However, for a counterexample of almost equal-sized interacting loops, see Hanaoka (1994).

Loop shrinkage factors.—The shrinkage factor of the loop length during the relaxation process after reconnection (eqs. [11]–[17]) is found to be in the range $q_2 = 0.95, \dots, 1.13$ (with a mean of $q_2 = 1.03 \pm 0.07$) for the large-scale field line and $q_1 = 0.93, \dots, 2.44$ (with a mean of $q_1 = 1.31 \pm 0.44$) for the small-scale loop. The latter ratio is particularly relevant for comparisons with the scaling ratio of maximum particle trajectories to flare loop half-lengths. If particles are accelerated in the cusp at beginning of recon-

nection, the time of flight (TOF) to the footpoints represents a measurement of the average field line length. In electron time-of-flight measurements based on energy-dependent HXR delays, the ratio of the TOF distance l^{TOF} to the flare loop half-length $s^{\text{loop}} = r_3(\pi/2)$ was found to be $l^{\text{TOF}}/s^{\text{loop}} = 1.43 \pm 0.30$ (Aschwanden et al. 1996), and $l^{\text{TOF}}/s^{\text{loop}} = 1.6 \pm 0.6$ (Aschwanden et al. 1999) with a different method, respectively. The agreement with the shrinkage factor of $q_1 = 1.31 \pm 0.44$ in the HXR-emitting small-scale flare loop is remarkable, considering the substantial correction factors that enter the electron time-of-flight distance (a mean factor of $q_x \approx 0.64$ for the pitch angle correction and a

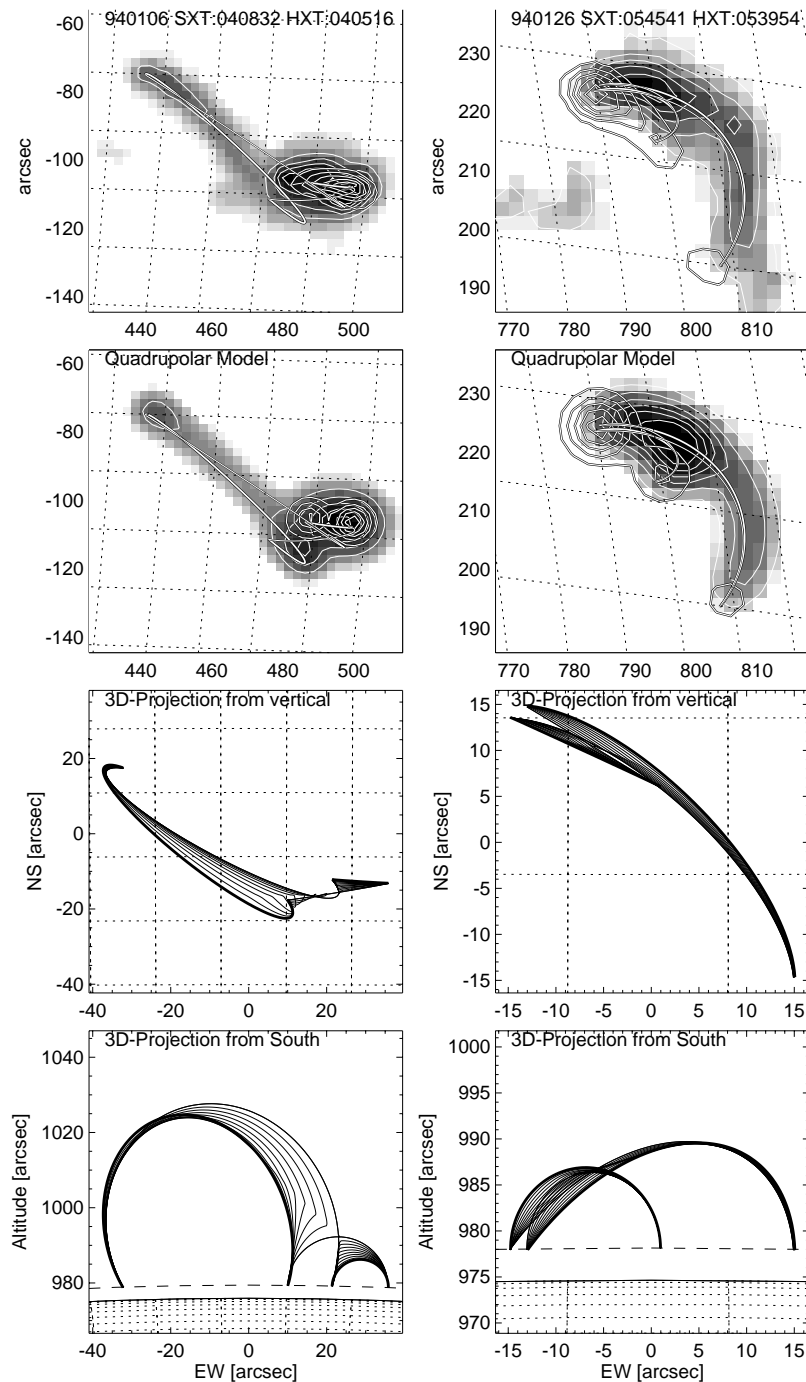


FIG. 3.—Continued

mean factor of $q_H \approx 0.85$ for the estimated helicity of magnetic field lines; see Appendices A and B in Aschwanden et al. 1996).

3.5. Application of Melrose's Quadrupolar Current-Loop Model

The three-dimensional geometry of our quadrupolar reconnection model is identical with the geometric setup of a theoretical model developed by Melrose (1997), wherein two current-carrying flux loops reconnect and form two new current-carrying flux loops between the original four footpoints. A fundamental assumption in Melrose's model is the conservation of the large-scale currents that flow

through coronal loops and close below the photosphere. A consequence of this assumption is that magnetic reconnection processes redistribute the current paths only, while the net current flowing into and out of the corona remains fixed. In Melrose's model, magnetic flux ($\Delta\Psi$) and electric current (ΔI) are transferred during reconnection, where the mutual inductance between the interacting flux loops depends on their geometry, relative distance, and preflare current. The most favorable case is when the final loops have zero initial flux and current and the initial loops have zero final flux and current, i.e., when all the flux and current is transferred from the initial (1, 2) to the final loops (3, 4). The maximum possible amount of magnetic energy ΔE^I

TABLE 2
 GEOMETRIC PARAMETERS OF QUADRUPOLEAR MODEL FOR 10 FLARES

PARAMETER	FLARE EVENT NUMBER									
	2	3	5	8	11	16	18	20	21	22
Solar Ephemerides										
Heliographic longitude of disk center l_0	346.56	229.43	299.31	24.02	113.13	23.23	349.89	184.87	58.49	154.25
Heliographic latitude of disk center l_0	4.37	6.88	7.24	4.61	-1.10	-5.88	0.10	0.96	-3.61	-5.58
Solar position angle P	3.77	17.78	23.41	24.91	9.58	-26.23	-13.03	16.39	-0.36	-9.67
Pre-Reconnection Loop 1										
Heliographic longitude l_1	23.17	253.25	258.76	69.71	167.22	84.78	20.05	104.36	88.78	209.16
Heliographic latitude b_1	-8.60	16.60	17.47	-24.38	-17.33	-6.35	-6.20	-21.46	-9.54	9.81
Azimuth angle \mathcal{S}_1	86.6	21.0	93.9	166.4	137.2	9.8	80.7	303.1	189.8	148.3
Loop radius r_1 (arcsec)	10.0	9.5	9.7	12.9	16.1	32.0	12.7	25.3	13.2	8.4
Pre-Reconnection Loop 2										
Heliographic longitude l_2	23.27	252.36	259.02	70.80	163.51	82.31	18.58	103.55	87.11	209.52
Heliographic latitude b_2	-9.26	16.42	16.82	-24.37	-18.14	-1.54	-7.19	-20.68	-8.49	9.17
Azimuth angle \mathcal{S}_2	99.9	18.8	115.8	182.2	16.9	292.5	20.6	295.0	331.2	136.9
Loop inclination angle ζ_2	-2.1	-11.9	-11.0	-3.3	-6.9	14.3	35.8	14.2	-10.7	-25.5
Loop radius r_2 (arcsec)	23.3	22.8	20.8	25.7	66.3	131.8	31.2	38.1	34.3	23.0
Loop center offset Δr_2 (arcsec)	-10.3	-7.3	-7.9	-2.5	-2.3	-60.2	6.6	-6.2	14.9	-10.2
Post-Reconnection Loop 3										
Heliographic longitude l_3	23.09	253.16	258.66	69.87	167.57	83.95	20.12	104.02	89.12	209.11
Heliographic latitude b_3	-8.61	16.62	17.37	-24.50	-17.49	-7.35	-6.75	-21.45	-9.38	9.78
Azimuth angle \mathcal{S}_3	93.9	26.7	106.6	173.7	125.7	327.4	47.8	290.7	176.5	154.9
Loop radius r_3 (arcsec)	9.9	8.1	8.4	10.0	10.1	20.9	4.7	22.4	7.3	8.8
Post-Reconnection Loop 4										
Heliographic longitude l_4	23.35	252.46	259.12	70.64	163.16	83.14	18.52	103.90	86.77	209.58
Heliographic latitude b_4	-9.25	16.40	16.92	-24.26	-17.98	-0.54	-6.64	-20.69	-8.64	9.21
Azimuth angle \mathcal{S}_4	96.4	16.9	109.3	178.1	21.0	302.7	35.8	302.4	320.6	133.9
Loop inclination angle ζ_4	-2.1	-11.9	-11.0	-3.3	-6.9	14.3	35.8	14.2	-10.7	-25.5
Loop radius r_4 (arcsec)	23.3	24.1	21.5	28.4	61.6	124.4	34.5	41.1	31.4	22.9
Loop center offset Δr_4 (arcsec)	-10.3	-7.3	-7.9	-2.5	-2.3	-60.2	6.6	-6.2	14.9	-10.2
Quadrupolar Angles										
Pre-reconnection angle $\mathcal{S}_{12} = \mathcal{S}_1 - \mathcal{S}_2$	-13.3	2.2	-21.9	-15.8	120.3	77.3	60.1	8.0	-141.5	11.4
Post-reconnection angle $\mathcal{S}_{34} = \mathcal{S}_3 - \mathcal{S}_4$	-2.6	9.9	-2.7	-4.4	104.7	24.7	12.0	-11.7	-144.1	21.0
Shear reduction $\Delta\mathcal{S} = \mathcal{S}_{34} - \mathcal{S}_{12} $	-10.8	7.6	-19.2	-11.4	-15.6	-52.6	-48.1	3.6	2.6	9.6
Scaling Ratios										
Pre-reconnection loop ratio r_2/r_1	2.33	2.41	2.14	2.00	4.10	4.11	2.46	1.51	2.59	2.75
Post-reconnection loop ratio r_4/r_3	2.36	2.98	2.57	2.85	6.08	5.95	7.39	1.83	4.28	2.59
Large loop shrinkage factor q_2	1.03	0.98	0.99	0.98	1.13	1.12	0.95	0.98	1.12	1.02
Small loop shrinkage factor q_1	0.96	1.04	1.08	1.10	1.32	1.39	2.44	1.02	1.51	0.93
Time-of-flight scaling ratio $l^{\text{TOF}}/s^{\text{loop}}$	1.14	1.11	1.50	1.51
Inductances (Melrose 1997)										
Self-induction of loop 1, L_1 (H)	17.66	16.67	17.10	22.73	28.45	56.46	22.37	44.59	23.30	14.72
Self-induction of loop 2, L_2 (H)	41.06	40.11	36.55	45.35	116.75	232.11	54.96	67.14	60.35	40.53
Self-induction of loop 3, L_3 (H)	17.40	14.29	14.78	17.54	17.83	36.80	8.22	39.53	12.90	15.54
Self-induction of loop 4, L_4 (H)	41.01	42.51	37.95	50.00	108.44	219.11	60.75	72.38	55.27	40.26
Mutual induction (loops 1, 2) $M_{1,2}$ (H)	6.11	5.13	5.40	6.74	-2.49	2.97	2.65	15.78	-4.05	4.68
Mutual induction (loops 1, 3) $M_{1,3}$ (H)	6.11	5.32	5.31	6.61	6.57	8.79	1.94	14.11	4.56	5.28
Mutual induction (loops 1, 4) $M_{1,4}$ (H)	6.17	5.46	5.78	7.56	-1.89	4.76	4.29	17.03	-2.82	4.63
Mutual induction (loops 2, 3) $M_{2,3}$ (H)	6.12	4.36	4.94	5.42	-0.64	5.04	1.06	14.90	-1.61	4.87
Mutual induction (loops 2, 4) $M_{2,4}$ (H)	14.46	14.54	13.02	16.64	39.44	77.53	19.08	24.18	19.73	14.25
Mutual induction (loops 3, 4) $M_{3,4}$ (H)	6.10	4.59	5.06	5.88	-0.43	4.80	1.19	15.20	-1.14	4.77
Irreducible reconnection M^{IR}	0.16	0.53	0.81	1.13	7.40	14.50	5.64	0.49	4.83	-0.36
Like current separation M_1^{LCS}	11.49	11.03	11.42	15.30	21.28	45.89	18.80	29.23	17.50	9.49
Like current separation M_2^{LCS}	26.59	26.33	24.00	30.03	75.46	152.51	37.47	43.83	38.18	26.09
Maximum free magnetic energy $\Delta E^f (10^{23} \text{ J})$	0.67	0.67	0.62	0.78	2.07	4.18	1.08	1.11	1.08	0.64

TABLE 2—Continued

PARAMETER	FLARE EVENT NUMBER									
	2	3	5	8	11	16	18	20	21	22
Flare Energies										
Magnetic energy (Melrose) $\log [\Delta E^I \text{ (ergs)}]$	29.83	29.83	29.79	29.89	30.32	30.62	30.03	30.04	30.03	29.81
SXR energy (<i>GOES</i>) $\log [\Delta E^{\text{SXR}} \text{ (ergs)}]$	29.16	29.04	29.24	29.01	29.19	29.81	28.66	29.86	29.00	28.84
HXR energy (HXT) $\log [\Delta E^{\text{HXR}} \text{ (ergs)}]$	29.41	29.62	29.79	29.17	29.87	30.37	29.77	30.14	29.83	29.70

available for a flare due to current transfer during reconnection, is calculated to be

$$\Delta E^I = \begin{cases} M_1^{\text{LCS}}(I_1 - I_2)I_2 + M^{\text{IR}}I_2^2, & \text{for } I_1 > I_2, \\ M_2^{\text{LCS}}(I_2 - I_1)I_1 + M^{\text{IR}}I_1^2, & \text{for } I_2 > I_1, \end{cases} \quad (22)$$

where M_i^{LCS} represent the like current separation (LCS) terms, which describe the effective change of mutual inductance when currents move apart or together,

$$M_i^{\text{LCS}} = M_{i1} + M_{i2} - M_{i3} - M_{i4}, \quad (23)$$

while M^{IR} represent the irreducible reconnection (IR) term, which includes currents that do not change and the parts that are transferred in the reconnection,

$$M^{\text{IR}} = \frac{1}{2}(L_1 + L_2 - L_3 - L_4) + M_{12} - M_{34}. \quad (24)$$

The self-inductance, L_i , of the i th loop (e.g., Landau & Lifshitz 1960, p. 139) is

$$L_i = M_{ii} = \mu_0 C_i r_i, \quad C_i = \left(\ln \frac{8r_i}{r_{\text{torus}}} - \frac{7}{4} \right), \quad (25)$$

where r_i is the major curvature radius of the i th loop, r_{torus} the cross-sectional torus radius of the current loop, and $\mu_0 = 4\pi \times 10^{-7} \text{ H m}^{-1}$ the vacuum permeability. Melrose (1997; the Appendix) approximated the mutual induction, M_{ij} , between two loops with major radii r_i and r_j , whose centers are separated by a distance d_{ij} and that are oriented at an angle \mathcal{S}_{ij} , (by)

$$M_{ij} = M_{ji} = \mu_0 (C_i C_j)^{1/2} \frac{8r_i^2 r_j^2 \cos \mathcal{S}_{ij}}{[(r_i + r_j)^2 + d_{ij}^2]^{3/2}} \\ = (L_i L_j)^{1/2} \left[\frac{2r_i r_j}{(r_i + r_j)^2 + d_{ij}^2} \right]^{3/2} \cos \mathcal{S}_{ij}, \quad (26)$$

where the factor C in equation (10) of Melrose (1997) is replaced by $(C_i C_j)^{1/2}$. Our notation differs from Melrose's by interchanged loop numerations (1 vs. 2), we denote the loop major radius by r_i (opposed to a_n in Melrose), and the loop minor torus radius by r_{torus} (opposed to r_n in Melrose). Another minor difference is that Melrose assumed semi-circular loops, while we allow for some inclination of the loop plane and an offset of the circular center for the large-scale loop here. However, our slightly more generalized geometry does not deviate significantly from the semi-circular approximation in many cases ($\Delta r_i \ll r_i$ and $\zeta_i \approx 0$) and is thus neglected in the following application. To estimate the energy of dissipated currents in a flare, we also need to know the preflare currents I_1 and I_2 of the interacting loops. Melrose estimated a current of $\Delta I = |I_1 - I_2| \approx 3 \times 10^{11} \text{ A}$, according to an observational current measurement by Leka et al. (1996), and used the detection limit for the smaller current, i.e., $\min(I_1, I_2) \lesssim$

10^{11} A . For our estimate we choose smaller currents, namely, $I_1 = 0.5 \times 10^{11} \text{ A}$ and $I_2 = 1 \times 10^{11} \text{ A}$ (or $\Delta I = |I_2 - I_1| = 0.5 \times 10^{11} \text{ A}$), which are found to be sufficient to explain the observed released flare energies. For most of the SXR flare loops (with typical radii of $r_2 \approx 25''$), we measured Gaussian half-widths of ≈ 2 SXT pixels, yielding torus radii of $r_{\text{torus}} \approx 5''$. For the largest loop, with a radius of $r_2 = 132''$, the torus radius was about 10 SXT pixels ($25''$). We adopt therefore a fixed ratio of $r_2/r_{\text{torus}} \approx 5$, yielding a constant value for the capacity, i.e., $C := C_i = \ln(8 \times 5) - 7/4 = 1.94$ (eq. [25]).

We calculate now the numerical values of dissipated currents in flares, ΔE^I , using equations (22)–(26) and the values r_i , \mathcal{S}_{ij} (eq. [5]), d_{ij} (eq. [6]) from our 10 analyzed flares. The distance d_{ij} between the loop centers, expressed in heliographic coordinates (l_i, b_i) , is obtained (using the cosine relation in a spherical triangle) from

$$d_{ij} = (r_{\odot} + h_{\text{min}}) \arccos [\cos(l_i - l_j) \cos(b_i - b_j)]. \quad (27)$$

The resulting self-induction terms L_i (eq. [25]), mutual induction terms M_{ij} (eq. [26]), the irreducible reconnection term M^{IR} , the like-current separation terms M_i^{LCS} (eq. [23]), and maximum free magnetic energies (for $I_2 > I_1$) are all listed in Table 2. We choose the case $I_2 > I_1$ in equation (22) because we find in all 10 flares that $M_2^{\text{LCS}} > M_1^{\text{LCS}}$, and thus $I_2 > I_1$ yields the larger amount of free energy ΔE^I than the case $I_1 > I_2$. The numerical values given in Table 2 show that the mutual induction terms M_{ij} are generally lower than the self-induction terms L_{ij} , which is physically intuitive because their relative distance d_{ij} is generally larger than their torus radii r_i or r_j (eq. [26]), in which case they would become comparable. Also one can see that the self-induction terms are largest for the longest loops (generally loop 2 and 4). The free magnetic energy available in a quadrupolar reconnection process is therefore determined by the self-induction of the largest loops that are involved in the process. The maximum amount of free energy is found to be of order $\Delta E^I \approx 0.6, \dots, 4 \times 10^{30} \text{ ergs}$, similar to the values estimated by Melrose (1997).

3.6. Estimates of Flare Energies

We now compare the theoretical values (or upper limits) of flare energies with observational estimates of released flare energies based on the *GOES* SXR flux and HXT hard X-ray flux. The *GOES* class corresponds to a logarithmic SXR flux, with $\text{C1.0} \mapsto 10^{-6} \text{ W m}^{-2}$, while M1.0 is a factor of 10 higher. The *GOES* class of our analyzed 10 flares ranges from C1.4 to M1.0 (see Table 1). Assuming an average temperature of $T = 15 \text{ MK}$ for the SXR plasma, we calculate the response per unit emission measure of the 1–8 Å *GOES* detector according to equation (9) of Thomas, Starr, & Crannell (1985; given here in their original

notation),

$$10^{55}b_8(T) = -3.86 + 1.17T - 0.0131T^2 + 0.000178T^3, \quad (28)$$

yielding $11.34 \times 10^{55} \text{ W m}^{-2}/\text{cm}^{-3}$, and we calculate the effective emission measure (with eq. [11] in Thomas et al. 1985) as

$$\text{EM} = 10^{55}B_8/[10^{55}b_8(T)] \text{ cm}^{-3}, \quad (29)$$

where B_8 is the reported *GOES* X-ray flux in units of W m^{-2} . This yields *GOES* emission measures in the range $\log[\text{EM} [(\text{cm}^{-3})]] = 48.09\text{--}48.95$. In a next step we estimate the volume of the SXR-emitting plasma during the flare, for which we take the torus volume of the smaller (SXR-brightest) flare loop,

$$V^{\text{SXR}} = (\pi r_{\text{torus}}^2)(\pi r_3), \quad (30)$$

yielding values in the range $\log(V^{\text{SXR}}) = 26.6\text{--}27.3 \text{ cm}^3$. Based on these values of the *GOES* emission measure EM and volume V^{SXR} , we obtain an estimate of the flare loop density n_e ,

$$n_e = \sqrt{\frac{\text{EM}}{V^{\text{SXR}}}}, \quad (31)$$

yielding values in the range $\log(n_e/\text{cm}^{-3}) = 10.8\text{--}11.2$. From this we can estimate the thermal energy contained in

the SXR-emitting flare plasma,

$$E^{\text{SXR}} = 3n_e k_B T V^{\text{SXR}}, \quad (32)$$

yielding thermal flare energies in the range $[\log(E^{\text{SXR}}/\text{ergs}) = 28.7\text{--}29.8]$. The individual values for each of the 10 flares are listed in Table 2.

Independently, we can estimate nonthermal flare energies based on the HXR count rates. Masuda (1994, Tables 3.1 and 3.2 therein) calculated for nine flares (with M1 count rates of $21\text{--}83 \text{ counts s}^{-1} \text{ SC}^{-1}$) energies of $4\text{--}90 \times 10^{27} \text{ ergs s}^{-1}$ in nonthermal electrons at energies greater than 20 keV. From these values we adopt an average conversion factor of $q_{\text{HXT}} = 4 \times 10^{26} \text{ ergs s}^{-1}$ per $C_{\text{HXT}} = 1 \text{ counts s}^{-1} \text{ SC}^{-1}$, ignoring variations of the spectral slope between different flares. The fluence or total released nonthermal energy can then be estimated by integrating the HXR flux over the flare duration Δt_{flare} (in seconds; listed in Table 1), which is approximately the product of the peak flux with the duration (for a triangular time profile)

$$E^{\text{HXR}} \approx q_{\text{HXT}} C_{\text{HXT}} \frac{\Delta t_{\text{flare}}}{2} \text{ ergs}. \quad (33)$$

The estimates of nonthermal flare energies so obtained are found in the range $\log(E^{\text{HXR}}) = 29.2\text{--}30.4 \text{ ergs}$. We show a correlation plot of the thermal (E^{SXR}) versus nonthermal flare energies (E^{HXR}) in Figure 4 (*upper left panel*). There is a clear correlation between the two energies and a close correspondence within a factor of ≈ 2 . (The lowest two non-thermal energies probably underestimate the equivalent of

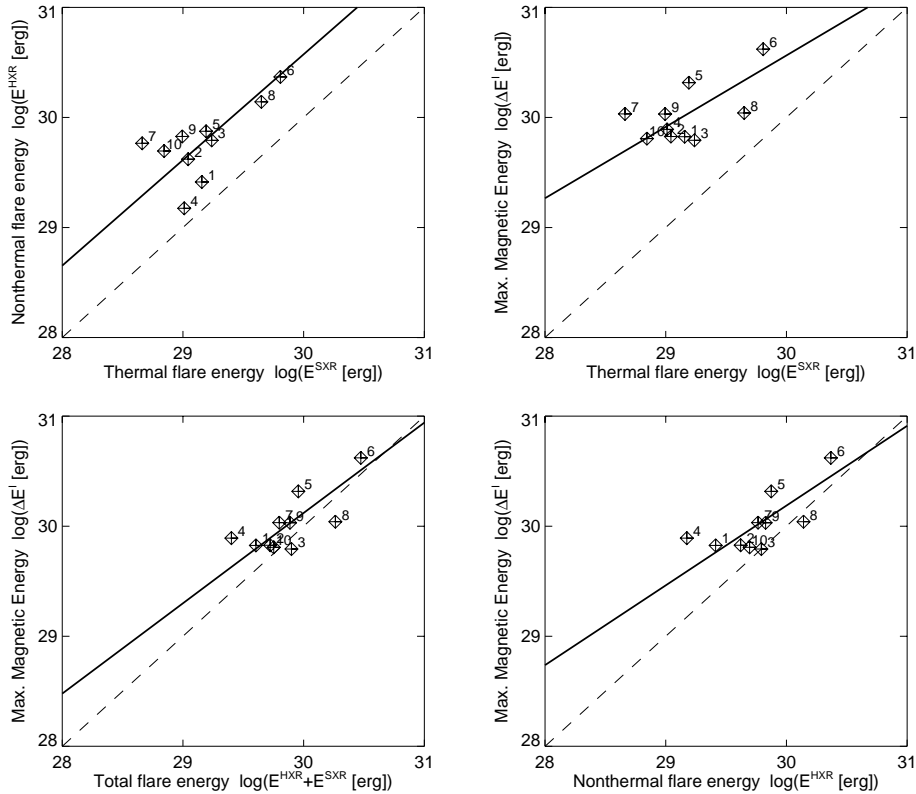


FIG. 4.—Correlation plots between the thermal flare energies E^{SXR} estimated from *GOES* fluxes, nonthermal flare energies E^{HXR} estimated from HXT fluxes, total energies $E^{\text{SXR}} + E^{\text{HXR}}$, and theoretical values of the maximum available free magnetic energy $\Delta E'$ in the framework of the quadrupolar current-loop model by Melrose (1997). The flares are numbered from 1 to 10 in chronological order. The dashed line indicates identical values, while the thick solid line shows a linear regression fit.

thermal energies because we did not correct for the steeper spectral slope that is inherent to weaker HXR count rates.) This correlation is another way to corroborate the Neupert effect, $I^{\text{SXR}}(t) \approx \int I^{\text{HXR}}(t) dt$ (Dennis & Zarro 1993). This agreement makes either (observational) energy estimate suitable for comparisons with theoretical energy estimates.

Based on these consistent observational flare estimates, we can now compare them with the theoretical values of the maximum free magnetic energy ΔE^I calculated in the framework of the quadrupolar flux transfer model by Melrose (1997). We show correlation plots with ΔE^I in Figure 4 separately for thermal energies E^{SXR} (Fig. 4, upper right panel), for nonthermal energies E^{HXR} (Fig. 4, lower right panel), and for total energies $E^{\text{SXR}} + E^{\text{HXR}}$ (Fig. 4, lower left panel). Although we have only a limited statistics of 10 events, there is a clear correlation evident between the theoretical values based on the Melrose (1997) model and the observational values estimated from SXR and HXR fluxes. Linear regression fits are also shown (according to the method of minimizing the orthogonal distance of data points to the linear fit). The correlation between theoretical and observational values is about as good as the correlation between the two independent observational values. We see that the chosen currents ($I_1 = I_2/2 = 0.5 \times 10^{11}$ A), the only free parameter in the theoretical model, is sufficient to balance the dissipated energies in SXR and HXR.

4. DISCUSSION

4.1. Reduction of the Quadrupolar Current-Loop Model of Melrose

Based on the statistics of 10 observed flare events we can evaluate the relative importance of various induction terms in Melrose's quadrupolar current-loop model. The numerical values of the induction terms (listed in Table 2) reveal that the largest contributions come from the longest flare loops (2 and 4). We show a correlation plot of the curvature radius r_2 of loop 2 with the maximum free energy ΔE^I in Figure 5. We find an excellent linear correlation between these two parameters, which can be fitted with the linear relation $\log(\Delta E^I) = 29.63 + \log(r_2/10^9 \text{ cm})$. This strong

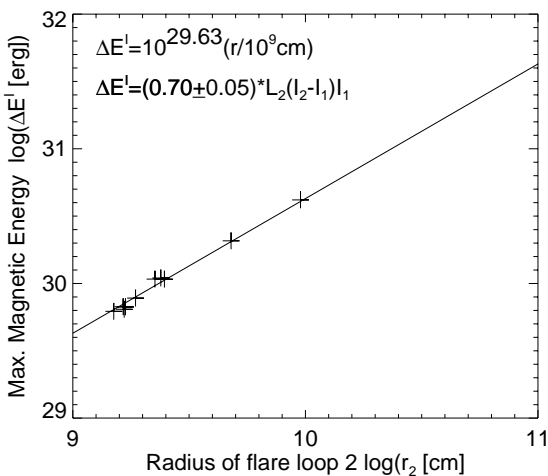


FIG. 5.—Linear regression fit between the maximum free magnetic energy ΔE^I given by Melrose (1997) and the radius r_2 , a proportionality factor in the self-induction term L_2 of the large-scale loop 2 (see discussion in § 4.1).

correlation suggests that the self-induction terms $L_2 = \mu_0 C_2 r_2$ (eq. [25]) and L_4 represent the dominant contributions, while other terms can be neglected. Also the terms M^{IR} are found to be much smaller than the term M_2^{LCS} . We can therefore reduce equation (22) to

$$\Delta E^I \approx M_2^{\text{LCS}}(I_2 - I_1)I_1 \approx L_2(I_2 - I_1)I_1. \quad (34)$$

For a fixed aspect ratio r_2/r_{torus} the capacity C is constant, i.e., $C = 1.94$ for $r_2/r_{\text{torus}} = 5$, and the self-induction L_2 is proportional to the loop curvature radius r_2 . Fitting this simplified relation (eq. [34]) with an empirical correction factor (to include all other neglected terms) to the accurate values of the energy ΔE^I , we find a best fit (Fig. 4, lower left panel) of

$$\begin{aligned} \Delta E^I &= (0.70 \pm 0.05)\mu_0 C r_2(I_2 - I_1)I_1 \\ &= 10^{29.63} \left(\frac{r}{10^9 \text{ cm}} \right) \text{ ergs}. \end{aligned} \quad (35)$$

where the right-hand approximation is based on average currents of ($I_2 - I_1 \approx I_1 \approx 0.5 \times 10^{11}$ A). This fit shows that the sum of all other neglected terms make up only $30\% \pm 5\%$ of the magnetic energy of the largest term L_2 (i.e., the self-induction term of loop 2). The values computed in Table 2 show clearly that the 30% reduction mainly comes from the mutual induction term M_{24} , the pair of longest field lines that stay relatively close to each other during reconnection and thus contribute the second most to the total inductance. Anyway, the approximation given in equation (35) allows us to estimate the maximum free magnetic energy with an accuracy of $\pm 7\%$, where we need to know only the curvature radius r_2 of the largest field line involved in the quadrupolar reconnection process. The physical implication of this result is that only the self-induction of the largest field line is relevant for the free magnetic energy available to a flare, which depends in first order on its curvature radius (or length) and the currents (I_1, I_2) of the two interacting field lines. The angle \mathcal{G}_{12} between the interacting field lines and their relative distance r_{12} is apparently of much less importance. The most favorable geometry is therefore dictated by the length of the larger field line only and hardly depends on the geometry or orientation of the smaller field line at all. This result was not anticipated in the various case studies calculated in Melrose (1997).

A numerical study to find the most favorable geometries in the framework of the Melrose (1997) model was performed by Hardy, Melrose, & Hudson (1997). In this parametric study, three footpoints were held fixed, while the position of the fourth footpoint was varied to find the maximum of energy transfer, for different current ratios I_2/I_1 . The most favorable configuration was always found for “parasitic magnetic topologies.” Interestingly, Hardy et al. (1997) found maximum energy transfer for a current ratio of $I_2/I_1 \approx 2$ (using a particular configuration with four fixed footpoints). This result can be explained analytically in terms of our “reduced Melrose model” (eq. [34]). Our reduced formula for maximum energy transfer states that the self-induction term L_2 of the largest loop is dominant, and thus maximum energy transfer is proportional to $\Delta E^I \propto (I_2 - I_1)I_1$ for $I_2 > I_1$ (eq. [34]), while the irreducible reconnection term with the proportionality $\Delta E^I \propto I_1^2$ can be neglected. If we ask, to which current loop I_1 most of the energy can be transferred from a given large-scale loop

with current I_2 , we find the most favorable combination just by evaluating the maximum of $\Delta E^I(I_1)$, i.e., by setting the derivative with regard to the variable I_1 equal to zero, i.e.,

$$\frac{\partial \Delta E^I}{\partial I_1} = \frac{\partial}{\partial I_1} L_2(I_2 - I_1)I_1 = L_2(I_2 - 2I_1) \equiv 0. \quad (36)$$

This yields the generally valid result of $I_2/I_1 = 2$ for the most favorable current ratio, confirming the numerical result found by Hardy et al. (1997) for a special case. Here-with we can also justify, in hindsight, our assumption of a current ratio $I_2/I_1 = 2$ for the numerical energy estimates calculated in § 3.5.

The analytical solution of the most favorable current ratio $I_2/I_1 = 2$ eliminates a further variable in the approximations of equations (34) and (35), and we can write an even simpler estimate for the maximum transferable flare energy,

$$\Delta E^I \approx L_2 \left(\frac{I_2}{2} \right)^2 \approx 10^{29.63} \left(\frac{r_2}{10^9 \text{ cm}} \right) \left(\frac{I_2}{10^{11} \text{ A}} \right)^2 \text{ ergs}, \quad (37)$$

which depends only on the radius r_2 and current I_2 of the large-scale field line involved in flaring. (This result justifies also eq. [26] in Melrose 1997). The size and orientation of the small-scale field line involved in the reconnection process does not matter in first order, and its current I_1 can be predicted to be the half-current of the large-scale field line, in the most favorable case.

4.2. Quadrupolar Reconnection Geometry

One of the oldest flare models on interacting flare loops is due to Gold & Hoyle (1960), with two side-by-side current-carrying loops of equal length with like-directed currents and oppositely directed magnetic fields. This geometry is not consistent with those observed here, where the loops have relative size ratios of 1:4 and none of them was found to be oriented in antiparallel direction.

The reconnection model of Heyvaerts, Priest, & Rust (1977) assumes that a current sheet builds up between emerging flux tubes and an oppositely directed overlying magnetic field, facilitating reconnection of the two field systems. The model has much in common with our three-dimensional quadrupolar reconnection model, except for its two-dimensional geometry visualized in simplified theoretical cartoons. However, even near-parallel magnetic field lines can cause a fairly efficient reconnection rate, e.g., the reconnection rate scales with $[\sin(\theta/2)]^{1/2}$ for Petschek reconnection (Soward 1982), as pointed out by the referee. The Heyvaerts et al. (1977) model gained a lot of popularity in recent studies where interacting flare loops were observed (e.g., Machado et al. 1988; Yokoyama & Shibata 1994; Hanaoka 1996, 1997; Nishio et al. 1997), although it was occasionally noted that the interacting flare loops were not oriented in antiparallel direction (e.g., Hanaoka 1996) as suggested in the two-dimensional model of Heyvaerts et al. (1977). Here we determined the angles between pre-reconnection field lines with a full three-dimensional model and found that none of the 10 cases was close to an antiparallel configuration: six cases were found to be nearly parallel (or collinear), while the other four cases had rather a nearly perpendicular orientation. The scenario of oppositely directed magnetic fields often considered in current-sheet topologies seems therefore not to be a crucial

requirement for magnetic reconnection, because nearly parallel or perpendicular fields seem to be equally efficient in facilitating magnetic reconnection, as inferred in the 10 cases here.

Sakai & DeJager (1991; see also review article by Sakai & DeJager 1996) proposed a more general approach, in which current coalescence for all possible orientations between interacting flare loops was considered, characterized as one-dimensional coalescence (if the interacting loops were nearly collinear and formed a one-dimensional l-shaped current sheet), two-dimensional coalescence (in the case of Y-shaped current sheets), and three-dimensional coalescence (in the case of X-point reconnection between nearly perpendicular oriented loops). While the numerical simulations of Sakai demonstrated that loop coalescence (or magnetic reconnection) works basically for all possible relative orientations, the explored geometries included mainly double loops of similar sizes, in contrast to the observed events here, where the interacting flare loops have typical size ratios of 1:4.

Quadrupolar reconnections have recently been theoretically explored with models that employ a magnetic charge topology (MCT; e.g., Sweet 1958; Baum & Bratenahl 1980; Gorbachev & Somov 1988; Longcope 1996, 1998) and were applied to magnetic topologies inferred from solar flares (e.g., Mandrini et al. 1993, 1996; Demoulin et al. 1993; VanDriel-Gesztelyi et al. 1994; Bagala et al. 1995; Longcope & Silva 1998). Because most of these theoretical models assume some spatial symmetry, such as equal sizes for interacting loops, they are not particularly relevant to the observed geometries, which involve rather strong asymmetries with typical loop size ratios of 1:4. MCT modeling is usually applied to the observed magnetic field topology, from which separator lines and separatrix surfaces are calculated. Such model fitting can localize the intersection of separatrices with the photosphere, but it appears that the primary small-scale flare loop (as identified by nonthermal particle signatures in HXR and radio, e.g., see Nishio et al. 1997), and thus the relevant topology of the actual reconnection site directly involved in the flare energy release, is not sufficiently resolved in present MCT models. A detailed comparison of an MCT model with an observed flare was presented in Longcope & Silva (1998), where the same magnitude of current ($I_1 = 0.5 \times 10^{11}$ A) was found as here to explain the energy content of accelerated electrons in the flare. However, the magnetic topology used for modeling the flare was more complex (with magnetogram partitioning into some 13 “magnetic islands”) than our basic quadrupolar scenario.

Let us mention some other theoretical and numerical MHD simulations with quadrupolar geometries. Uchida et al. (1998) studied large-scale quadrupolar configurations with spatial symmetry across the neutral line, which are not applicable to the flares observed by Hanaoka (1996) and Nishio et al. (1997). Karpen et al. (1995, 1998) performed 2.5 MHD simulations of driven reconnection in symmetrically and asymmetrically sheared arcades. The latter study (Karpen et al. 1998) with asymmetric dipoles comes closest to geometries of interest here. These simulations are capable of reproducing the evolution of shear-driven reconnection, leading to fragmented current sheets that deform into magnetic islands. Kliem (1994) simulated particle acceleration in the environment of such magnetic islands (X- and O-points), providing an important “missing link” between

reconnection theory and observational signatures in the form of nonthermal particles, as they are observed in HXR and radio during a flare. Somov, Kosugi, & Sakao (1998) and Uralov (1996) discussed further applications of quadrupolar geometries to solar flares.

4.3. Large-Scale Currents

Melrose (1997) emphasized the important role played by large-scale currents in solar flare energy release. Observational evidence of currents in coronal loops was presented in recent work by, e.g., Gary & Demoulin (1995), Wang, Xu, & Zhang (1994b), and Leka et al. (1996). Gary & Demoulin (1995) inferred total currents of $I = 0.5 \times 10^{13}, \dots, 1.5 \times 10^{14}$ A per active region, which would supply 100–3000 flare-prone loops per active region. Wang et al. (1994b) derived similar large currents ($I = 3.0, \dots, 8.5 \times 10^{12}$ A) in active region 5747. They also noted that most flares are not located at the sites of maximum vertical currents but at the edges, as did Canfield et al. (1992). Leka et al. (1996) analyzed emerging bipoles and found evidence that the emerging flux tubes are already twisted and current-carrying before emergence, having currents of $I = 2, \dots, 5 \times 10^{11}$ A. Note that this current attributed to single (emerging) flux tubes is 4–10 times larger than required to explain the flare energies observed here.

Because the foregoing studies demonstrate that the amount of observed large-scale currents in active region loops and in emerging flux tubes is sufficient to supply the required free magnetic energy released in flares, as estimated from SXR and HXR fluxes, the model of reconnection-driven magnetic flux transfer as quantified by Melrose (1997) can be considered as a sensible approach. A next question is whether the observed locations of concentrated vertical currents coincides with flare footpoint locations. Canfield et al. (1992) noted that the peaks of the vertical electrical current density distribution in AR 6919 were not coincident with the HXR location of the 1991 November 15 flare. Despite additional analysis of electron precipitation sites from H α locations and SXR flare loops, no compelling spatial correlation between the sites of vertical current and flare loops was found (Canfield et al. 1993; Metcalf et al. 1994; Li et al. 1997). We would like to offer a solution to “Canfield’s dilemma” in the framework of our quadrupolar reconnection model (Melrose 1997). Large-scale currents are present in an arbitrary number of active region loops, which can be transferred or redistributed over different current paths if some form of magnetic reconnection takes place, e.g., if an emerging flux tube rises against the overlying field. Once a local reconnection process is initiated, a part, but not necessarily all, of the flux can be transferred to a flare loop, making a well-defined upper limit of magnetic energy available for flare energy release, i.e., $\Delta E^I \approx 0.7L_2(I_2 - I_1)I_1$ (eq. [35]). Because the amount of effectively consumed magnetic energy in the primary flare loop can be significantly smaller than the maximum available transferable current, the location of the peak current density does not change dramatically during the flare, especially when the current in the large-scale field line is stronger ($I_2 > I_1$) and when the footpoint displacement is small ($r_1 \ll r_2$). Furthermore, the quadrupolar reconnection model predicts that the outcome produces two disjoint flare loops, and thus the dominant (nonthermal) HXR sources, which are tied to the (chromospheric) footpoints of the small-scale flare loop, are necessarily displaced from the

footpoints of the large-scale flare loop, which may be rooted in regions of high vertical current densities. The relative displacements (between footpoint positions 2– and 1– in Fig. 1) is of the order of the half-size of the smaller flare loop, i.e., $r_1/2 = 5''\text{--}16''$ for our analyzed 10 events. Furthermore, because the existing large-scale currents exceed the flare requirements by far, there is no need that flares are associated with loops that carry the maximum detected currents. We expect therefore no spatial correlation between HXR locations and the location of the peak current density in an active region. Even if the loop with the strongest large-scale current is involved in a flare, we expect a displacement of $\approx 5''\text{--}16''$ from the nearest HXR footpoint.

4.4. Shear Angle of Flaring Loops

Shearing of the magnetic field is considered in some flare models (e.g., Sturrock 1966) as the principal driving force to build up the nonpotential magnetic energy required for flaring (see § 2.5). A high shear angle (defined by the deviation from a dipolar field direction across the neutral line in the flaring region) has been invoked to represent an important, if not necessary, condition for flaring (Hagyard et al. 1984, 1990). Also, bright SXR loops, which may indicate heating processes below a flare threshold, are preferentially found near to strong-shear segments of the neutral line (Falconer 1997; Falconer et al. 1997). Numerical MHD simulations of sheared arcades have also demonstrated that sufficient energy can be built up to supply flares (Klimchuk et al. 1988; Klimchuk & Sturrock 1992). The general expectation is that a flare instability dissipates nonpotential magnetic energy, and thus the relaxed postflare configuration should converge to a potential field. A clear-cut case of such a relaxation process to a potential field during a flare was shown by Sakurai et al. (1992). However, in some cases, magnetic shear was observed to increase after a flare (Wang et al. 1994a). How does this relate to our quadrupolar reconnection model? Our measurement procedure quantifies the relative angles between pre-reconnection field lines and post-reconnection field lines. However, the magnetic geometry is simplified to circular segments, so that the angles defined by the footpoint baselines are not necessarily consistent with the effective angle between coronal field lines, especially when the field lines are helically twisted. Nevertheless we obtained an average shear reduction of $\Delta\theta \approx 10^\circ\text{--}50^\circ$ for flares with nearly vertical loop planes, which is consistent with the expectation of shear-driven flare models (e.g., Sturrock 1966).

Another quantity we reconstructed was the angle between pre-reconnection field lines, which turned out to be near perpendicular in five cases, and nearly collinear in the other five cases. If we assume that the neutral line be oriented orthogonal to the large-scale field line, then the high-shear condition postulated by Hagyard et al. (1984) is not a necessary flare condition. Chen et al. (1994) also reported that that about one-half of the observed flares occur with mean shear angles of $< 50^\circ$, and thus strong shear does not seem to be a necessary condition for flaring. Actually, we found that the maximum amount of released flare energies depends in first order on the self-induction of the secondary flare loop, which is proportional to its length and the product of the currents of the interacting flare loops but is almost independent of the relative orientation of the interacting flare loops. This is another indication that the initial shear angle does not necessarily warrant a high probability

for flaring. If emerging flux pushes small-scale field lines against the overlying large-scale field, the condition for reconnection is fulfilled, regardless what the shear angle happens to be.

5. CONCLUSIONS

While a number of theoretical concepts envisioning quadrupolar magnetic reconnection have been applied to solar flares previously, often in the form of cartoons, virtually no attempt has been made so far to determine the actual three-dimensional geometry of reconnecting field lines directly from observations. In this study we report geometric measurements to deduce the exact three-dimensional geometry of reconnecting field lines in 10 flare events, from SXR and HXR observations made by *Yohkoh*. In our three-dimensional model we approximate the pre-reconnection field lines with a dipole-like geometry (fitted by circular segments), while the newly configured field lines undergo a transition from cusp shaped (circular segments) to a dipole-like geometry. This model provides also a quantitative formulation of the change of shear angles (between the interacting flare loops), the shrinkage of field line lengths during the post-reconnection relaxation process, as well as all geometric parameters that are necessary to calculate self-induction and mutual induction terms between current-carrying loops. These numerical data are suitable to apply the Melrose (1997) quadrupolar current-loop model, from which we compare the predicted maximum free magnetic energy available for flare energy release with actually observed energy contents in SXR and HXR emission. The major results of this study are summarized in the following.

1. The quadrupolar geometry fitted to observed pairs of (disjoint) flare loops, which are interpreted as outcome of a quadrupolar reconnection process, yields for all analyzed events a geometric solution for two pre-reconnection field lines, which are required to intersect each other near the top of the smaller flare loop.

2. The curvature ratio of the pre-reconnection field lines is found to be $r_2/r_1 = 2.6 \pm 0.9$ and becomes larger for the post-reconnection field lines, i.e., $r_4/r_3 = 3.9 \pm 1.9$. This strong asymmetry in reconnecting loop sizes is consistent with the scenario in which newly emerging small-scale loops interact with preexisting large-scale loops.

3. The pre-reconnection field lines are oriented almost collinear ($\mathcal{G}_{1,2} < 22^\circ$) in half of the cases and nearly perpendicular ($60^\circ < \mathcal{G}_{1,2} < 141^\circ$) in the other half of the cases. This configuration is not inconsistent with the antiparallel configuration visualized in simplified cartoons of the Heyvaerts et al. (1977) model, because some reconnection modes are also efficient for near-parallel fields. After reconnection, the relative shear angle reduces generally by $\Delta\mathcal{G} \approx -10^\circ, \dots, 50^\circ$. These results are essentially consistent with the notion that energy release in flares dissipates non-potential magnetic energy and in this way reduces the relative magnetic shear.

4. The geometric length of the large-scale field line does generally not significantly change during reconnection: the length ratio before and after reconnection is found to be $q_2 = 1.03 \pm 0.07$. However, the small-scale field line generally undergoes a shrinkage by a factor of $q_1 = 1.31 \pm 0.44$ during dipolar relaxation in the post-reconnection phase. This scaling ratio is also consistent with time-of-flight measurements of electron trajectories, which scale with the dipolar SXR flare loop half-length s as $l^{\text{TOF}}/s = 1.43 \pm 0.30$

(Aschwanden et al. 1996) or $l^{\text{TOF}}/s = 1.6 \pm 0.6$ (Aschwanden et al. 1999), respectively. The agreement of these two scaling ratios suggest that nonthermal electrons are accelerated near the cusp of newly reconnected field lines.

5. Using the Melrose (1997) flare model of current-carrying loops, we calculate the self-induction and mutual induction terms between the four pre-reconnection and post-reconnection field lines and find that the self-induction L_2 of the large-scale field line dominates all other induction terms, so the maximum free magnetic energy available for flare energy release because of magnetic flux and current transfer scales in first order with the curvature radius r_2 of the large-scale loop, i.e., $\Delta E^I \approx 0.7\mu_0 Cr_2(I_2 - I_1)I_1$. The maximum transferred magnetic energy occurs for a current ratio of $I_2/I_1 = 2$. For a group of reconnecting small-scale loops with some current distribution $f(I_1)$, those loops that have one-half the current of the overlying field lines ($I_1 = I_2/2$) receive most of the transferred energy via self-induction of the large-scale field lines and are thus favored for flaring. This reduction of Melrose's theory leads to a simple expression for the available free magnetic energy in flares, i.e., $\Delta E^I \approx 10^{29.63}(r/10^9 \text{ cm})(I_2/10^{11} \text{ A})^2$ ergs, regardless of the dimension and orientation of the small-scale loop. This theoretical expression for the available free magnetic energy is indeed found here to correlate with observed flare energy contents based on SXR and HXR fluxes. This correlation strongly supports the Melrose (1997) postulate that the large-scale currents circulating through coronal loops and closing below the photosphere cannot be dissipated in the corona but are merely redistributed over different current paths during a magnetic reconnection process, where the magnetic energy associated with the net current transfer before and after reconnection (which is essentially an ideal MHD process) represents a sensitive measure for the amount of flare energy converted into fluid motion, heating, and acceleration of particles.

6. The outcome of a quadrupolar reconnection process is two disjoint flare loops. The displacement between these two disjoint flare loops, of which the smaller one converts most of the magnetic energy and produces nonthermal HXR and radio signatures while the larger one carries more current ($I_2 > I_1$) in the most favorable case for the small-scale loop, can explain Canfield's dilemma (Canfield et al. 1992), showing why the maximum of the vertical currents does not coincide with the centroids of HXR, SXR and H α flare signatures.

7. The three-dimensional quadrupolar geometry implies cusp-shaped field lines in the initial phase after X-type reconnection and thus can also serve as a model for cusp-shaped flare geometries (e.g., Tsuneta et al. 1992; Forbes & Acton 1996). Cusp-shaped single-loop flares can be considered, as an alternative to the conventional helmet-streamer geometry, as a special case of quadrupolar reconnection, where the secondary large-scale loop is undetected in SXR and radio while the visibility of the small-scale flare loop is perhaps enhanced by ongoing reconnection in adjacent new field lines.

In this study we explored the three-dimensional geometry of reconnecting field lines from suitable flare data, i.e., by selecting cases with interacting flare loops. The resulting geometric parameters allowed us to apply the quadrupolar model of current-carrying loops by Melrose (1997), which provided crucial new physical insights into the flare energy release process. While this first part of a paper series is entirely

focused on the determination of the three-dimensional geometry, future work is planned on analysis of magnetic data, modeling of particle dynamics such as acceleration and propagation (HXR and radio), and heating processes (SXR).

We acknowledge valuable comments and discussions with David Alexander, Nariaki Nitta, Bernhard Kliem,

Arnold Benz, and Hugh Hudson. We thank the anonymous referee for helpful critical comments. This work was supported by NASA *Yohkoh*/SXT contract NAS 8-40108. The HXR data used in this paper are taken by the *Yohkoh* mission of ISAS, Japan, which was prepared and is operated by the international collaboration of Japanese, US, and UK scientists under the support of ISAS, NASA, and PPARC, respectively.

APPENDIX

SOLAR LOOP COORDINATE TRANSFORMATIONS

We define the geometry of a circular loop i in the solar corona with 7 free parameters: the position of the midpoint of the loop footpoint baseline, expressed in heliographic coordinates (l_i, b_i) and a reference height level h_{\min} above the solar surface, the loop curvature radius (r_i) , the offset of the circular center from the footpoint baseline (Δr_i) , the azimuthal angle between the footpoint baseline and the east-west direction (counterclockwise), also called tilt angle (\mathcal{G}_i) , and the inclination angle of the loop plane to the vertical (ζ_i) . The height of footpoints of coronal loops is assumed to be at the top of the chromosphere, for which we assume $h_{\min} \approx 2500$ km, which reduces the loop parameters to 6. For the special case of semicircular loops $(\Delta r_i = 0)$ with vertical loop planes $(\zeta_i = 0)$, the number of loop parameters reduces to 4.

We introduce a parametrization of loop points (x_L, z_L) as function of the circular angle φ in the loop plane (x_L-z_L) plane, which depends only on the loop radius r_i and circular offset Δr_i ,

$$x_L(\varphi) = r_i \cos \varphi, \quad \varphi_{0,i} \leq \varphi \leq (\pi - \varphi_{0,i}), \quad (\text{A1})$$

$$z_L(\varphi) = r_i(\sin \varphi - \sin \varphi_{0,i}), \quad (\text{A2})$$

$$\varphi_{0,i} = -\arcsin(\Delta r_i/r_i), \quad (\text{A3})$$

where the offset Δr_i is defined positive if the circular loop center is located above the footpoint baseline. In a next step we apply two rotations (by azimuthal angle \mathcal{G}_i and inclination angle ζ_i) in order to express the loop coordinates in a coordinate system (x, y, z) that is co-aligned with the heliographic coordinate system,

$$\begin{pmatrix} x \\ y \\ z \end{pmatrix} = \begin{pmatrix} \cos \mathcal{G} & -\sin \mathcal{G} & 0 \\ \sin \mathcal{G} & \cos \mathcal{G} & 0 \\ 0 & 0 & 1 \end{pmatrix} \begin{pmatrix} 1 & 0 & 0 \\ 0 & \cos \zeta & \sin \zeta \\ 0 & -\sin \zeta & \cos \zeta \end{pmatrix} \begin{pmatrix} x_L \\ 0 \\ z_L \end{pmatrix}. \quad (\text{A4})$$

Wrapping the surface plane $(x-y)$ parallel to the solar surface, the curvature of the solar surface is automatically considered in all following transformations, in such a way that the footpoints have always the same height h_{\min} above the solar surface. The loop coordinates (x, y, z) can now easily be transformed into heliographic coordinates (l, b) and distance from the sun center r ,

$$\begin{pmatrix} l \\ b \\ r \end{pmatrix} = \begin{pmatrix} l_1 + \arctan [x/(z + h_{\min} + r_{\odot})] \\ b_1 + \arctan [y/(z + h_{\min} + r_{\odot})] \\ (z + h_{\min} + r_{\odot}) \end{pmatrix}. \quad (\text{A5})$$

The spatial scales of the coordinates (x_L, z_L) , (x, y, z) and (r) are specified in the same physical units as r_i , Δr_i , h_{\min} , r_{\odot} , e.g., in km or arcseconds. If arcseconds are used as spatial units, the spatial scale of 1 arcsecond corresponds to $(1 \text{ AU}) \times 2\pi / (360^\circ \times 60' \times 60'') = 723 \text{ km}$ ($1 \text{ AU} = 149.6 \times 10^6 \text{ km}$) and varies by about 3% between summer and winter. The midpoint of the loop baseline is now centered at $(l = 0, b = 0)$ at an altitude of h_{\min} above the solar surface.

The transformation of loop coordinates into an image that maps the plane of the sky oriented to celestial north, we have to apply four additional rotations: (1) to rotate the loop center to heliographic latitude b_1 , (2) to rotate the loop center to heliographic longitude difference $(l_0 - l_1)$, (3) to tilt the solar equator by b_0 , and (4) to align the solar axis with celestial North (or the y -axis of the image),

$$\begin{pmatrix} X \\ Y \\ Z \end{pmatrix} = \begin{pmatrix} \cos(P + P_0) & -\sin(P + P_0) & 0 \\ \sin(P + P_0) & \cos(P + P_0) & 0 \\ 0 & 0 & 1 \end{pmatrix} \begin{pmatrix} 1 & 0 & 0 \\ 0 & \cos(b_0) & -\sin(b_0) \\ 0 & \sin(b_0) & \cos(b_0) \end{pmatrix} \\ \times \begin{pmatrix} \cos(l_0 - l) & 0 & -\sin(l_0 - l) \\ 0 & 1 & 0 \\ \sin(l_0 - l) & 0 & \cos(l_0 - l) \end{pmatrix} \begin{pmatrix} 1 & 0 & 0 \\ 0 & \cos(-b) & -\sin(-b) \\ 0 & \sin(-b) & \cos(-b) \end{pmatrix} \begin{pmatrix} 0 \\ 0 \\ r \end{pmatrix}. \quad (\text{A6})$$

The following ephemerides are needed for this transformation: the longitude l_0 and latitude b_0 of the solar disk center, and the (counterclockwise) position angle P_0 of the solar axis at the time of observations. The angle P represents the rotation angle by which the image has been rotated with respect to celestial North. For solar images that have already aligned the solar axis with the y -axis of the image, this angle is $P = -P_0$, after roll-angle correction. The coordinates (X, Y) represent now image

coordinates measured in east-west and NW direction relative to the Sun's center, in the same units as the chosen units for r_i , Δr_i , h_{\min} , r_{\odot} . The coordinate Z represents the line-of-sight distance of a loop point from the plane of sky through the center of the Sun.

REFERENCES

- Aschwanden, M. J. 1999, in Proc. Nobeyama Symposium on Solar Physics with Radio Observations, ed. T. S. Bastian, N. Gopalswamy, & K. Shibasaki (NRO Rep.; Nagano: Nobeyama Radio Obs.), in press
- Aschwanden, M. J., Fletcher, L., Sakao, T., Kosugi, T., & Hudson, H. 1999, *ApJ*, 517, 977
- Aschwanden, M. J., Kosugi, T., Hudson, H. S., Wills, M. J., & Schwartz, R. A. 1996, *ApJ*, 470, 1198
- Bagala, L. G., Mandrini, C. H., Rovira, M. G., Demoulin, P., Henoux, J. C. 1995, *Sol. Phys.*, 161, 103
- Baum, P. J., & Bratenahl, A. 1980, *Sol. Phys.*, 67, 245
- Benz, A. O. 1985, *Sol. Phys.*, 96, 357
- . 1993, *Plasma Astrophysics, Kinetic Processes in Solar and Stellar Coronae* (Dordrecht: Kluwer)
- Canfield, R. C., et al. 1992, *PASJ*, 44, L111
- . 1993, *ApJ*, 411, 362
- Chen, J., Wang, H., Zirin, H., & Ai, G. 1994, *Sol. Phys.*, 154, 261
- Demoulin, P., Van Driel-Gesztelyi, L., Schmieder, B., Henoux, J. C., Csepura, G., & Hagyard, M. J. 1993, *A&A*, 271, 292
- Dennis, B. R. 1985, *Sol. Phys.*, 100, 465
- Dennis, B. R., & Zarro, D. M. 1993, *Sol. Phys.*, 146, 177
- Duijveman, A., Hoyng, P., & Machado, M. E. 1982, *Sol. Phys.*, 81, 137
- Falconer, D. 1997, *Sol. Phys.*, 176, 123
- Falconer, D., Moore, R. L., Porter, J. G., Gary, G. A., & Shimizu, T. 1997, *ApJ*, 482, 519
- Forbes, T. G., & Acton, L. W. 1996, *ApJ*, 459, 330
- Gary, G. A., & Demoulin, P. 1995, *ApJ*, 445, 982
- Gold, T., & Hoyle, F. 1960, *MNRAS*, 120, 7
- Gopalswamy, N., Raulin, J. P., Kundu, M. R., Nitta, N., Lemen, J. R., Herrmann, R., Zarro, D., & Kosugi, T. 1995, *ApJ*, 455, 715
- Gorbachev, V. S., & Somov, B. V. 1988, *Sol. Phys.*, 150, 77
- Hagyard, M. J., Smith, J. B., Jr., Teuber, D., & West, E. A. 1984, *Sol. Phys.*, 91, 115
- Hagyard, M. J., Venkatakrishnan, P., & Smith, J. B., Jr. 1990, *ApJS*, 73, 159
- Hanaoka, Y. 1994, *ApJ*, 420, L37
- . 1996, *Sol. Phys.*, 165, 275
- . 1997, *Sol. Phys.*, 173, 319
- . 1999, *PASJ*, in press
- Hardy, S. J., Melrose, D. B., & Hudson, H. S. 1997, *Publ. Astron. Soc. Australia*, 15, 318
- Heyvaerts, J., Priest, E. R., & Rust, D. M. 1977, *ApJ*, 216, 123
- Karpen, J. T., Antiochos, S. K., & DeVore, C. R. 1995, *ApJ*, 450, 422
- Karpen, J. T., Antiochos, S. K., DeVore, C. R., & Golub, L. 1998, *ApJ*, 495, 491
- Kliem, B. 1994, *ApJS*, 90, 719
- Klimchuk, J. A., & Sturrock, P. A. 1992, *ApJ*, 385, 344
- Klimchuk, J. A., Sturrock, P. A., & Yang, W. H. 1988, *ApJ*, 335, 456
- Kosugi, T., et al. 1991, *Sol. Phys.*, 136, 17
- Kundu, M. R., Nitta, N., White, S. M., Shibasaki, K., Enome, S., Sakao, T., Kosugi, T., & Sakurai, T. 1995, *ApJ*, 454, 522
- Landau, L. D., & Lifshitz, E. M. 1960, *Electrodynamics of Continuous Media* (Oxford: Pergamon Press)
- Leka, K. D., Canfield, R. C., McClymont, A. N., & VanDriel-Gesztelyi, L. 1996, *ApJ*, 462, 547
- Li, J., Metcalf, T. R., Canfield, R. C., & Wülser, J.-P. 1997, *ApJ*, 482, 490
- Longcope, D. W. 1996, *Sol. Phys.*, 169, 91
- . 1998, *ApJ*, 507, 433
- Longcope, D. W., & Silva, A. V. R. 1998, *Sol. Phys.*, 179, 349
- Machado, M. E., Moore, R. L., Hernandez, A. M., Rovira, M. G., Hagyard, M. J., & Smith, J. B., Jr. 1988, *ApJ*, 326, 425
- Mandrini, C. H., Demoulin, P., VanDriel-Gesztelyi, L., Schmieder, B., Cauzzi, G., & Hofmann, A. 1996, *Sol. Phys.*, 168, 115
- Mandrini, C. H., Rovira, M. G., Demoulin, P., Henoux, J. C., Machado, M. E., & Wilkinson, L. K. 1993, *A&A*, 272, 609
- Masuda, S. 1994, Ph.D. thesis, Univ. Tokyo
- Melrose, D. B. 1997, *ApJ*, 486, 521
- Metcalf, T. R., Canfield, R. C., Hudson, H. S., Mickey, D. L., Wuelser, J. P., Martens, P. C. H., & Tsuneta, S. 1994, *ApJ*, 428, 860
- Nakajima, H., Dennis, B. R., Hoyng, P., Nelson, G., Kosugi, T., & Kai, K. 1985, *ApJ*, 288, 806
- Nishio, M., Yaji, K., Kosugi, T., Nakajima, H., & Sakurai, T. 1997, *ApJ*, 489, 976
- Press, W. H., Flannery, B. P., Teukolsky, S. A., & Vetterling, W. T. 1986, *Numerical Recipes, The Art of Scientific Computing* (Cambridge: Cambridge Univ. Press)
- Sakai, J. I., & DeJager, C. 1991, *Sol. Phys.*, 134, 329
- . 1996, *Space Sci. Rev.*, 77, 1
- Sakurai, T., Shibata, K., Ichimoto, K., Tsuneta, S., & Acton, L. W. 1992, *PASJ*, 44, L123
- Sato, J., Kosugi, T., & Makishima, K. 1999, *PASJ*, 51, 127
- Sato, J., Sawa, M., Masuda, S., Sakao, T., Kosugi, T., & Sekiguchi, H. 1998, *The Yohkoh HXT Image Catalogue* (Nagano: Nobeyama Radio Obs./NAO)
- Somov, B. V., Kosugi, T., & Sakao, T. 1998, *ApJ*, 497, 943
- Soward, A. M. 1982, *J. Plasma Phys.*, 28, 415
- Strong, K. T., et al. 1984, *Sol. Phys.*, 91, 325
- Sturrock, P. A. 1966, *Nature*, 5050, 695
- Sweet, P. A. 1958, *Nuovo Cimento Suppl.*, 8, 188
- Sylwester, J., & Sylwester, B. 1998, in *ASP Conf. Ser. 155, Three-Dimensional Structure of Solar Active Regions*, ed. C. E. Alissandrakis & B. Schmieder (San Francisco: ASP), 381
- Thomas, R. J., Starr, R., & Crannell, C. J. 1985, *Sol. Phys.*, 95, 323
- Tsuneta, S., Hara, H., Shimizu, T., Acton, L. W., Strong, K. T., Hudson, H. S., & Ogawara, Y. 1992, *PASJ*, 44, L63
- Tsuneta, S., et al. 1991, *Sol. Phys.*, 136, 37
- Uchida, Y., et al. 1998, *Ap&SS*, in press
- Uralov, A. M. 1996, *Sol. Phys.*, 168, 311
- VanDriel-Gesztelyi, L., Hofmann, A., Demoulin, P., Schmieder, B., & Csepura, G. 1994, *Sol. Phys.*, 149, 309
- Wang, H., Ewell, M. W., Jr., Zirin, H., & Ai, G. 1994a, *ApJ*, 424, 436
- Wang, H., Gary, D. E., Zirin, H., Schwartz, R. A., Sakao, T., Kosugi, T., & Shibata, K. 1995, *ApJ*, 453, 505
- Wang, T., Xu, A., & Zhang, H. 1994b, *Sol. Phys.*, 155, 99
- Yokoyama, T., & Shibata, K. 1994, *ApJ*, 436, L197